FINAL REPORT

Aluminide Coatings for Power-Generation Applications

Contract Number 4000007035

Submitted by: Ying Zhang
Department of Mechanical Engineering
TTU Box 5014
115 W 10th Street
Tennessee Technological University
Cookeville, TN 38505-0001

Collaborators: B. A. Pint, J. A. Haynes, I. G. Wright, and P. F. Tortorelli
Metals and Ceramics Division
Oak Ridge National Laboratory
Oak Ridge, TN 37831-6156

November, 2003

Table of Content

Executive Summary

Aluminide coatings are of interest for many high temperature applications because of the possibility of improving the oxidation of structural alloys by forming a protective external alumina scale. In order to develop a comprehensive lifetime evaluation approach for aluminide coatings used in fossil energy systems, some of the important issues have been addressed in this report for aluminide coatings on Fe-based alloys (Task I) and on Ni-based alloys (Task II).

In Task I, the oxidation behavior of iron aluminide coatings synthesized by chemical vapor deposition (CVD) was studied in air + 10vol.% H_2O in the temperature range of 700-800°C and the interdiffusion behavior between the coating and substrate was investigated in air at 500-800°C. Commercial ferritic (Fe-9Cr-1Mo) and type 304L (Fe-18Cr-9Ni, nominally) austenitic stainless steels were used as the substrates. For the oxidation study, the as-deposited coating consisted of a thin (<5μm), Al-rich outer layer above a thicker (30-50μm), lower Al inner layer. The specimens were cycled to 1000 1-h cycles at 700°C and 500 1-h cycles at 800°C, respectively. The CVD coating specimens showed excellent performance in the water vapor environment at both temperatures, while the uncoated alloys were severely attacked. These results suggest that an aluminide coating can substantially improve resistance to water vapor attack under these conditions. For the interdiffusion study, the ferritic and austenitic steels were coated with relatively thicker aluminide coatings consisting of a 20-25μm outer layer and a 150-250μm inner layer. The composition profiles before and after interdiffusion testing (up to 5,000h) were measured by electron probe microanalysis (EPMA). The decrease of the Al content at the coating surface was not significant after extended diffusion times (≤ 5,000h) at temperatures ≤ 700ºC. More interdiffusion occurred at 800ºC in coatings on both Fe-9Cr-1Mo and 304L alloys; a two-phase microstructure was formed in the outer coating layer on 304L after interdiffusion of 2,000h at 800°C. The interdiffusion behavior was simulated using a computer model COSIM (Coating Oxidation and Substrate Interdiffusion Model), which was originally developed for MCrAlY overlay coatings by NASA. Complimentary modeling work using a mathematic model from Heckel et al. also was conducted. Reasonable agreement was observed between the simulated and experimental composition profiles, particularly for aluminide coatings on Fe-9Cr-1Mo ferritic steels.

In Task II, the research focused on the CVD aluminide bond coats for thermal barrier coatings (TBC). The martensitic phase transformation in single-phase β-NiAl and (Ni,Pt)Al coatings was studied and compared. After isothermal exposure to 1150°C for 100 hours, the β phase in both types of coatings was transformed to a martensite phase during cooling to room temperature. Martensitic transformation also was observed in the (Ni,Pt)Al bond coat with and without the ceramic top layer after thermal cycling at 1150°C (700 1-h cycles). Such transformation resulted from Al depletion in the coating due to the formation of the Al_2O_3 scale on coating surface and interdiffusion between the coating and superalloy substrate. The volume changes associated with the martensitic transformation could affect the coating surface stability ("rumpling") and thus contributing to TBC failure. To elucidate the effect of Hf levels in the superalloy

substrate on the oxidation performance, directionally-solidified René 142 superalloys containing three different Hf contents with and without aluminide coatings were cyclically oxidized at 1100 and 1150°C in air. Poor scale adhesion was observed for all bare and NiAl-coated René 142 superalloys, as compared with single-crystal superalloys such as René N5. Spallation occurred at relatively early stages disregarding the Hf contents in the superalloys. Finally, a platinum plating system has been set up at Tennessee Technological University to carefully control the Pt plating process for synthesizing (Ni,Pt)Al and other Pt-containing coatings. The effects of the Pt electroplating parameters such as plating current density on Pt adhesion and uniformity were examined. The plating rate increased nearly linearly with the increased current density from 0.2 to 0.6A/dm^2. More Pt was built up near the specimen edges/corners than on the flat surface at high current density; the thicker Pt near specimen edges/corners over the flat surfaces led to localized spallation of the Pt layer in these areas.

Task I. Aluminide Coatings on Fe-based Alloys

1.1. The Effect of Water Vapor on the Oxidation Behavior of CVD Iron Aluminide Coatings [*]

1.1.1. Introduction

Increasing the temperature capabilities of ferritic and austenitic alloys for advanced power generation applications has been of ongoing interest for many years due to potential gains in energy efficiency and concomitant decreases in emissions. In particular, it is hoped to be able to use 9-12%Cr steels up to 650°C or higher, and 300-series stainless steels to 700°C or higher. These classes of alloys owe their oxidation resistance to the formation of Cr-containing oxides which, especially for the ferritic steels, become less protective at higher temperatures and in water vapor or steam environments so that protective coatings will have to be considered.[1, 2] Iron aluminides are well known to have excellent oxidation and sulfidation resistance at high temperatures due to the formation of an external, protective alumina scale.[3-6] Also, alumina scales are expected to be less affected than are Cr-containing scales by water vapor-containing environments. While there are concerns about the mismatch of the coefficient of thermal expansion (CTE) between these substrate alloys and Fe_3Al, (~13.0 x 10^{-6}°C^{-1} for ferritic alloys, ~19.0 x 10^{-6}°C^{-1} for austenitic alloys, and ~20.5 x 10^{-6}°C^{-1} for Fe_3Al in the temperature range of 700-800°C),[7] aluminide coatings could be a good candidate for improving the oxidation resistance of ferritic and austenitic steels provided that they can be applied with the desired composition and microstructure.[8]

In order to understand the considerations involved in forming the desired coating, and their performance, a laboratory chemical vapor deposition (CVD) reactor at Oak Ridge National Laboratory (ORNL) is being used to maximize control of the coating fabrication process.[7, 9] It is expected that the coating parameters identified could readily be translated to commercial pack processing,[10] and that same guidance could be provided for other coating processes. One ferritic (Fe-9Cr-1Mo) and one austenitic alloy (304L) were selected as the substrate materials. With a well-controlled laboratory CVD procedure, the coatings can be made uniform in composition, purity and microstructure over the entire substrate. Previous work considered the hot corrosion behavior of these aluminide coatings in H_2S-containing environment and their isothermal oxidation performance in air + H_2O.[7] In the present work, the focus has been to investigate the cyclic oxidation behavior of the Fe-Al coated steels in the temperature range of 700-800°C in air + 10vol.% H_2O. A cyclic oxidation test with a 1h cycle time was used as an accelerated test. Upon cooling after each cycle at temperature, the stresses developed between the protective oxide and the coating (from oxide growth and CTE mismatch) and between the coating and substrate (from CTE differences) will eventually become sufficient to cause the scale to crack or spall. Since any damage to the external alumina scale must be repaired upon reheating in order to maintain corrosion protection during additional cycles, the coating must contain sufficient Al to reform the protective surface

[*] A paper based on this part has been submitted to *Oxid. Met.*, 2003.

oxide or accelerated attack may occur. Results based on specimen mass changes and microstructural characterization indicated that a thin aluminide coating could substantially improve the resistance of these chromia-forming alloys to water vapor attack.

1.1.2. Experimental Procedures

The substrates used in this study were a ferritic alloy, Fe-9Cr-1Mo and an austenitic stainless steel 304L,[6] and their compositions are given in Table 1. While these particular alloys may have insufficient strength for the application of interest, they are considered to be reasonably representative of the basic compositions of the two alloy classes of interest. The CVD coating apparatus and coating method have been described previously.[7, 9] The substrate alloys were aluminized for 6 hours at a reactor temperature of 900°C and a reactor pressure of 13.3 kPa. Because the target coatings contained less Al than many of the Fe_3Al type of compositions previously investigated,[3-6] model Fe-Al alloys containing 13at.% (7wt.%), 15at.% (8wt.%) and 20at.% (11wt.%) Al (+0.05at.%Hf) were cast and tested in the same oxidation tests for comparison. The Hf additions were made to improve the resistance to scale spallation. All specimens were polished to a 0.3μm alumina finish and were ultrasonically cleaned in acetone and methanol prior to CVD coating, or subsequent oxidation tests. The coated specimens were exposed in the oxidation tests with as-deposited surfaces.

Table 1. The compositions of substrate alloys.

Alloy	Fe-9Cr-1Mo		304L	
	wt.%	at.%	wt.%	at.%
Fe	88.46	87.75	69.70	68.59
Cr	9.26	9.87	18.29	19.33
Ni	0.16	0.15	8.75	8.19
Al	<0.01	--	<0.01	--
Mo	0.96	0.55	0.24	0.14
Ce	<0.01	--	<0.01	--
Co	0.02	0.02	0.18	0.17
Cu	0.07	0.06	0.29	0.25
Mn	0.47	0.47	1.84	1.84
Si	0.19	0.37	0.47	0.92
V	0.23	0.25	0.10	0.11
Nb	0.05	0.03	--	--
Ti	<0.01	--	<0.01	--
Hf	<0.01	--	<0.01	--
Zr	<0.01	--	<0.01	--
P	0.013	0.0233	0.021	0.0373
B	0.001	0.0051	0.001	0.0051
C	516 ppm	0.2380	204 ppm	0.0933
N	480 ppm	0.1899	790 ppm	0.3100
O	26 ppm	0.0090	49 ppm	0.0168
S	8 ppm	0.0014	33 ppm	0.0057

Cyclic oxidation testing in air + 10vol.% H_2O was conducted to 1000 cycles at 700°C and to 500 cycles at 800°C in an automated test rig with a cycle consisting of 1h at temperature and 10min cooling at room temperature. Distilled water was atomized into the flowing air stream above its condensation temperature and heated to the test temperature within the alumina tube. Both ends of the vertical furnace tube were closed and the water exiting the rig was condensed, collected and used to calibrate the amount of injected water. (Very little of the H_2O was consumed by the oxidation reactions.) Specimens were removed from the rig at fixed intervals and weighed to develop mass change-time data. Before and after exposure, selected specimens were examined by light microscopy, field emission gun scanning electron microscopy (FEG-SEM) equipped with energy-dispersive spectroscopy (EDS), X-ray diffraction (XRD), and electron probe microanalysis (EPMA). The corrosion products on specimens for cross-sectional examination were protected by Cu-plating the specimen prior to mounting in epoxy.

1.1.3. Results

Figure 1(a) shows a back-scattered electron image of a cross-section of the as-deposited CVD aluminide coating on Fe-9Cr-1Mo. It consisted of a ~3µm thick outer layer and a ~55µm thick inner layer. An EPMA composition profile, as reported previously,[7] from the outer coating surface into the substrate indicated that the outer layer contained ~20%Al (all compositions are given in at.% hereafter, unless specified otherwise), and that there was a gradual decrease in the Al content through the rest of the coating thickness. The concentration of Cr was relatively uniform throughout the whole coating, at approximately 8-9%.

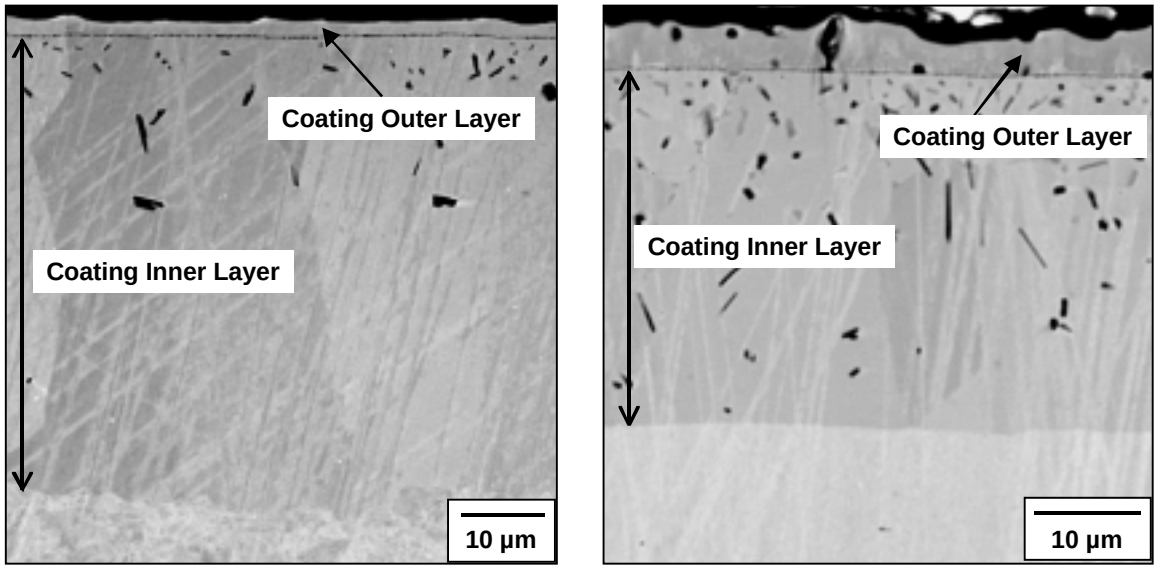

Fig. 1. EPMA back-scattered electron images of the as-deposited CVD aluminide coating on (a) Fe-9Cr-1Mo and (b) 304L.

Figure 1 (b) shows a cross-section of the as-deposited coating on 304L stainless steel. In this case, the presence of Ni in the substrate resulted in a more complicated

microstructure. The outer layer was ~5μm, slightly thicker than that on the ferritic substrate. The EPMA composition profile of the coating indicated that the outer layer was enriched in Ni (>20%) and contained more Al (~35%) than the outer layer on Fe-9Cr-1Mo.[7] However, the inner layer on 304L was only ~35μm thick, and it also contained more Al than on Fe-9Cr-1Mo. The Cr content, on the other hand, was ~6% in the outer layer, but increased to 18-19% in the inner layer. The total thickness of the coating (outer layer + inner layer) was thinner on 304L (~40μm) than that on the Fe-9Cr-1Mo alloy (~58μm) by the same CVD coating procedure. This difference can be attributed to slower diffusion in the austenitic substrate.[11]

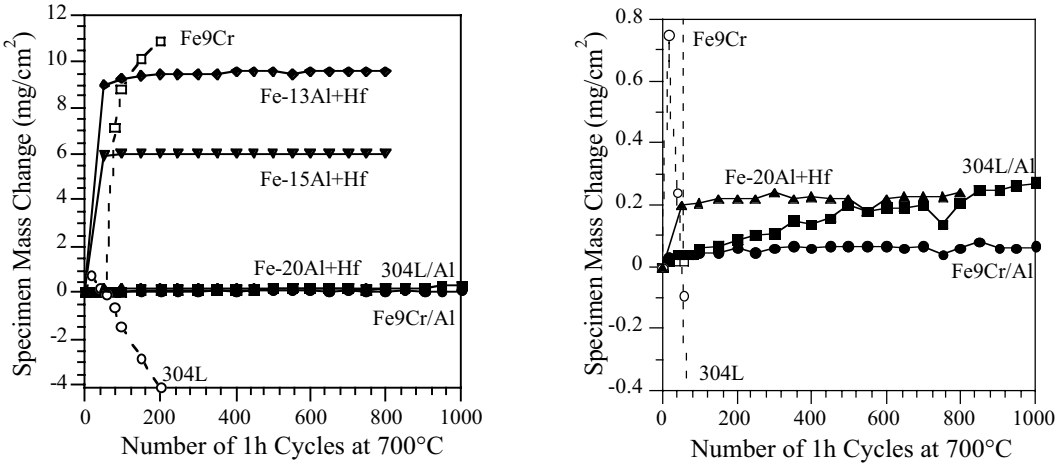

Fig. 2. Specimen mass changes during 1h cycles at 700°C in air + 10vol.% H_2O; in (b), selected data from (a) are replotted over a smaller ordinate range. "Fe9Cr/Al" and "304L/Al" denote data for aluminized Fe-9Cr-1Mo and 304L, respectively.

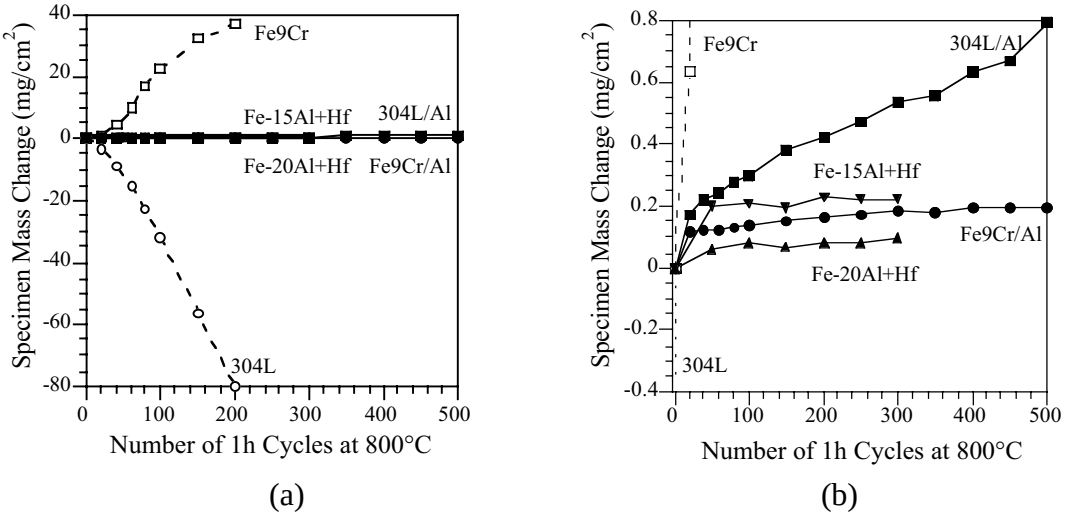

Fig. 3. Specimen mass changes during 1h cycles at 800°C in air + 10vol.% H_2O; in (b), selected data from (a) are replotted over a smaller ordinate range. "Fe9Cr/Al" and "304L/Al" denote data for aluminized Fe-9Cr-1Mo and 304L, respectively.

The mass change results for cyclic oxidation testing in air + 10vol.% H_2O at 700°C and 800°C are shown in Figures 2 and 3, respectively, which clearly indicate the benefit of aluminide coatings on both steel alloys in this temperature regime. For uncoated Fe-9Cr-1Mo, a high mass gain resulted from Fe_2O_3 formation (as identified by XRD), Figures 2(a) and 3(a). This type of rapid attack would not be anticipated in a dry air environment. In contrast, uncoated 304L showed high mass losses during 200, 1-h cycles, at each temperature. Mass gains or losses of uncoated Fe-9Cr-1Mo and 304L at 800°C were obviously higher than at 700°C after the same number of cycles (200 cycles), as expected. Figures 2(b) and 3(b) plot the same test results but over a smaller ordinate range. CVD aluminized alloys registered relatively small mass gains; the mass gains of aluminized 304L were higher than aluminized Fe-9Cr-1Mo at both testing temperatures.

For cast Fe-Al alloys with 13~20%Al, there appeared to be an initial transient period with a high rate of increasing in mass gain, followed by a steady state regime where the mass gain was almost constant during further thermal cycling to the end of the test (Figures 2 and 3). The transient mass gain decreased with increased Al content in the alloys at both temperatures, which suggests that alloys with higher Al contents can more rapidly form a protective Al-rich oxide layer. For a given Al content, e.g. 15% and 20% Al, lower final mass gains were measured at 800°C than at 700°C. This was probably due to faster Al diffusion within the alloy at the higher temperature, allowing a protective oxide to form more quickly.

The surface morphologies of the ferritic and austenitic alloys with and without CVD aluminide coatings after cyclic oxidation in air + 10vol.% H_2O are shown in Figures 4-6. The uncoated Fe-9Cr-1Mo formed a very fine-structured scale at 700°C, Figure 4(a), while massive Fe_2O_3 nodules were observed on the surface at 800°C, Figure 4(c) (note the difference in magnification marker). Very smooth scales were formed on the coated Fe-9Cr-1Mo at 700°C and 800°C, Figures 4(b) and 4(d), except that isolated nodules were found occasionally on the coated Fe-9Cr-1Mo at 800°C, as shown in Figure 5. The uncoated 304L spalled severely at both temperatures, as shown in Figures 6(a) and (c), while the surfaces of the aluminized 304L, Figures 6(b) and (d), appeared uniform and smooth after thermal cycling. (Note the difference in magnification between micrographs of uncoated and coated specimens.)

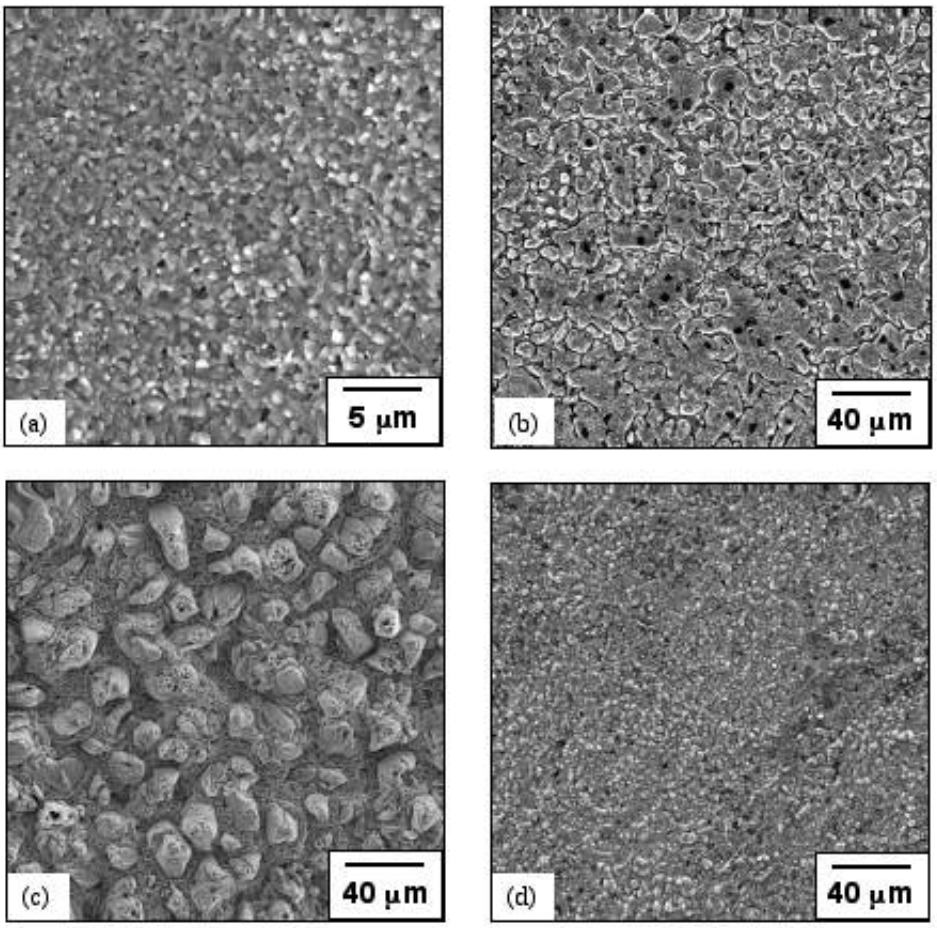

Fig. 4. SEM secondary electron images of surface morphologies of Fe-9Cr-1Mo with and without aluminide coatings after thermal cycling in air + 10vol.% H_2O: (a) without an aluminide coating after 200 1-h cycles at 700°C; (b) with an aluminide coating after 1000 cycles at 700°C; (c) without an aluminide coating after 200 cycles at 800°C; (d) with an aluminide coating after 500 cycles at 800°C.

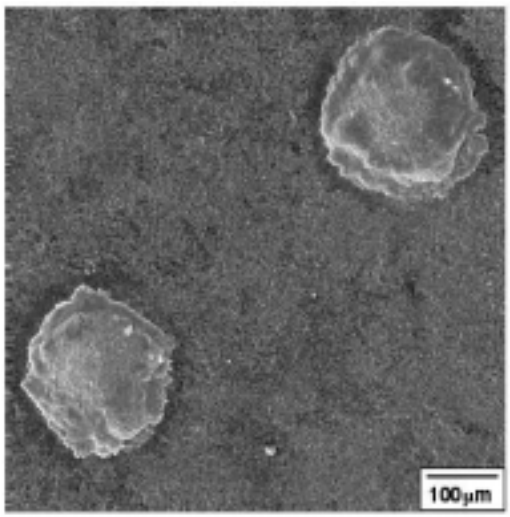

Fig. 5. SEM secondary electron image showing isolated nodules formed on coated Fe-9Cr-1Mo after 500 cycles at 800°C in air + 10vol.%H_2O.

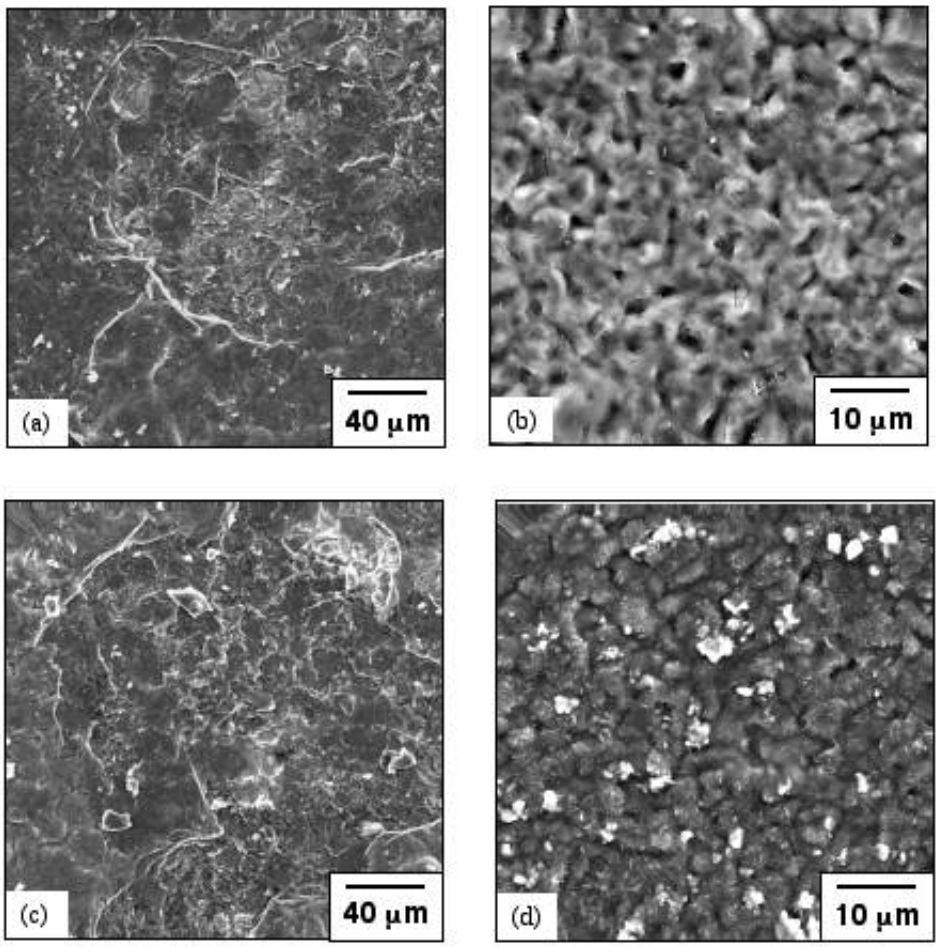

Fig. 6. SEM secondary electron images of surface morphologies of 304L with and without aluminide coatings after thermal cycling in air + 10vol.% H_2O: (a) without an aluminide coating after 200 1-h cycles at 700°C; (b) with an aluminide coating after 1000 cycles at 700°C; (c) without an aluminide coating after 200 cycles at 800°C; (d) with an aluminide coating after 500 cycles at 800°C. Note that spallation was obvious on uncoated 304L.

The benefit of aluminide coatings on both alloys with respect to water vapor attack is more evident from cross-sections of the specimens after exposure. Figures 7(a) and (b) compare the SEM secondary electron images of cross-sections of uncoated and CVD aluminized Fe-9Cr-1Mo after cyclic oxidation at 700°C in air + 10vol.%H_2O. A thick duplex structure was observed on uncoated Fe-9Cr-1Mo after 200 cycles at 700°C, with predominantly Fe_2O_3 in the outer scale and Fe-Cr mixed oxides in the inner layer, Figure 7(a). A similar structure was observed on uncoated Fe-9Cr-1Mo at 800°C; in this case, the outer Fe_2O_3 scale was delaminated from the inner oxide where Cr could be detected in addition to Fe, as indicated in Figure 7(c). On the other hand, a very thin and adherent oxide was formed on the aluminized Fe-9Cr-1Mo at 700°C (after 1000 cycles) and 800°C (after 500 cycles), as shown in Figures 7(b) and (d). The oxide scales at some locations appeared to penetrate the thin aluminide outer coating [white arrows in Figure

7(b)], but not the underlying layer and most of the coating remained intact. Figure 8 shows a back-scattered electron image and the corresponding X-ray maps of O, Al, Cr, Fe and N after cyclic oxidation testing at 800°C in the coated Fe-9Cr-1Mo, the same specimen in Figure 7(d). A continuous aluminum oxide was formed on aluminized Fe-9Cr-1Mo after exposure to 800°C water vapor. There were a few Cr-rich precipitates in the coating and in the substrate, Figure 8(d). The Al-rich acicular particles concentrated near the substrate-coating interface were rich in N, as indicated in Figure 8(c) and 8(f). Similar distributions of O, Al, Cr and Fe also were found on the oxidized Fe-9Cr-1Mo coating specimen at 700°C.

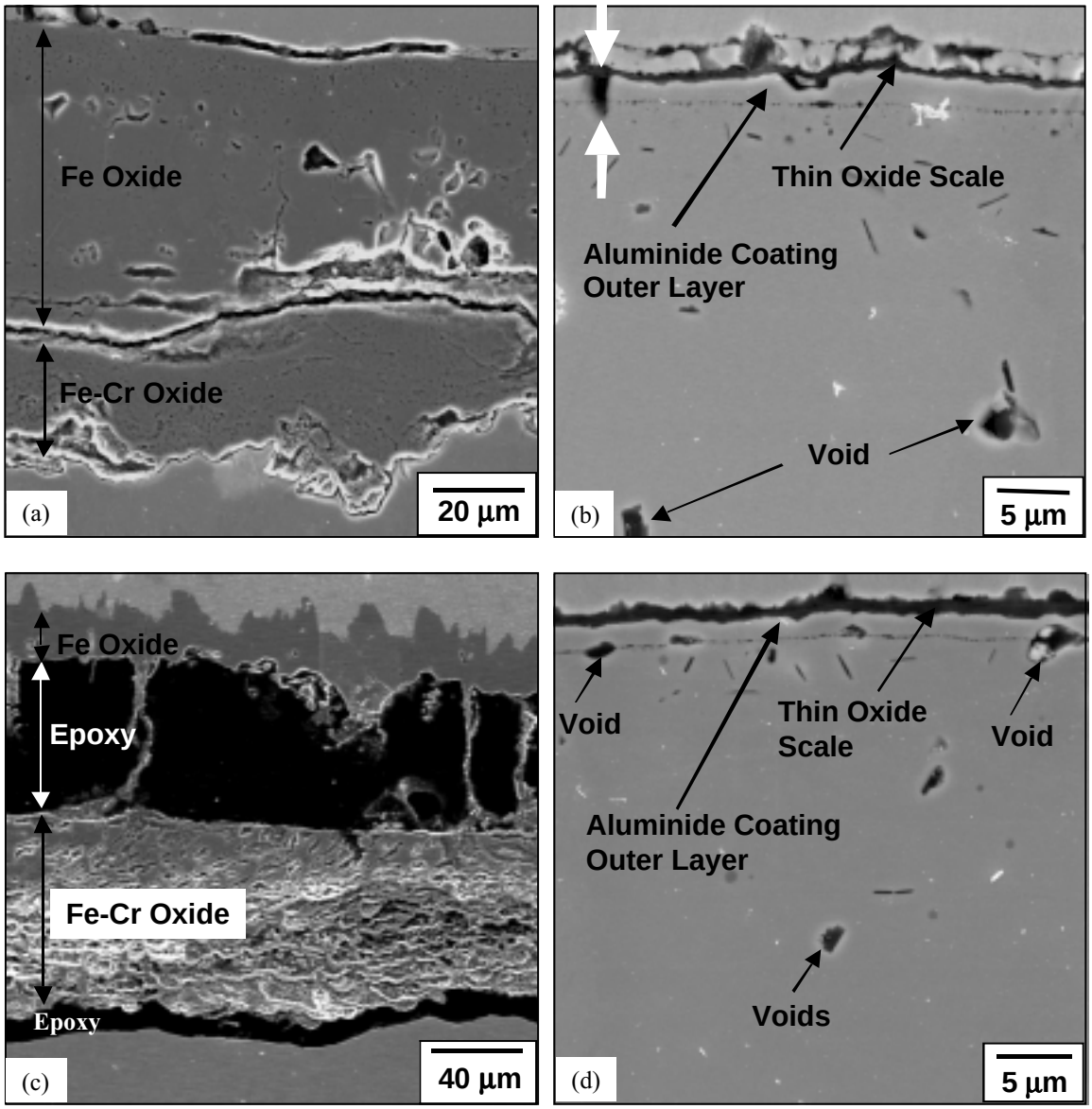

Fig. 7. SEM secondary electron images of cross-sections of Fe-9Cr-1Mo with and without aluminide coatings after thermal cycling in air + 10vol.% H_2O: (a) without a coating after 200 1-h cycles at 700°C; (b) with a coating after 1000 cycles at 700°C, white arrows indicating oxide penetration; (c) without a coating after 200 cycles at 800°C; (d) with a coating after 500 cycles at 800°C.

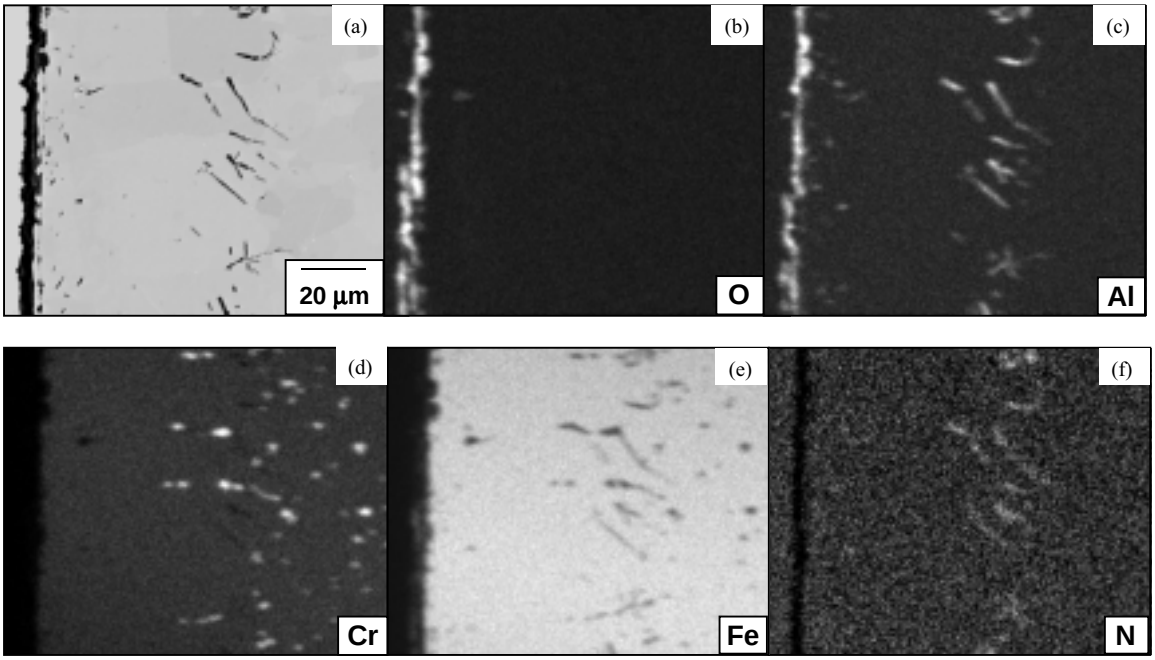

Fig. 8. (a) EPMA back-scattered electron cross-sectional image of coated Fe-9Cr-1Mo after 500 1-h cycles at 800°C in air + 10vol.% H_2O. X-ray maps of the same region showing (b) O, (c) Al, (d) Cr, (e) Fe, and (f) N.

For uncoated 304L, the cross-sections were very similar after 200 cycles at 700°C and 800°C, with Fe-rich oxide in the outer scale, and mixed Fe-Cr-Ni oxides in the inner layer, Figures 9(a) and (c). For coated 304L, thin oxide scales were formed on the top of the aluminide coatings, <2µm at 700°C and ~3µm at 800°C, respectively, as shown in Figures 9(b) and (d). The oxide scales on coated 304L were in general thicker than on coated Fe-9Cr-1Mo after the same amount of exposure, which is consistent with mass change results, Figures 2(b) and 3(b). Figure 10 shows a back-scattered electron image and the corresponding X-ray maps of O, Al, Ni, Cr, and Fe after thermal cycling at 800°C in the coated 304L. The O and Al maps indicate a continuous surface aluminum oxide with little oxygen penetration into the coating. The Ni and Al maps show Ni-Al precipitates in the coating and an enrichment of both elements near the coatings surface underneath the oxide scale. The maps of Ni and Cr indicate that the inner coating layer consisted of Ni-rich and Cr-rich phases after exposure to 800°C. A similar distribution of these elements was also observed on the coated 304L after exposure at 700°C. When observed at a higher magnification, a two-phase microstructure (dark-gray and light-gray phases) was noticed in the outer coating layer on 304L after exposure at both temperatures, and an example is shown in Figure 11. EDS analysis indicated that the dark phase was rich in Al and Ni while the light phase contained less Al and Ni but rich in Fe. A similar two-phase microstructure has been observed in an aluminized 304L with a thicker outer layer (~25µm) after isothermal oxidation for 2000h at 800°C;[12] the composition measured by EPMA is 40Al-40Ni-17-Fe-3Cr for the dark phase and 9Al-4Ni-73Fe-14Cr for the light phase, respectively.

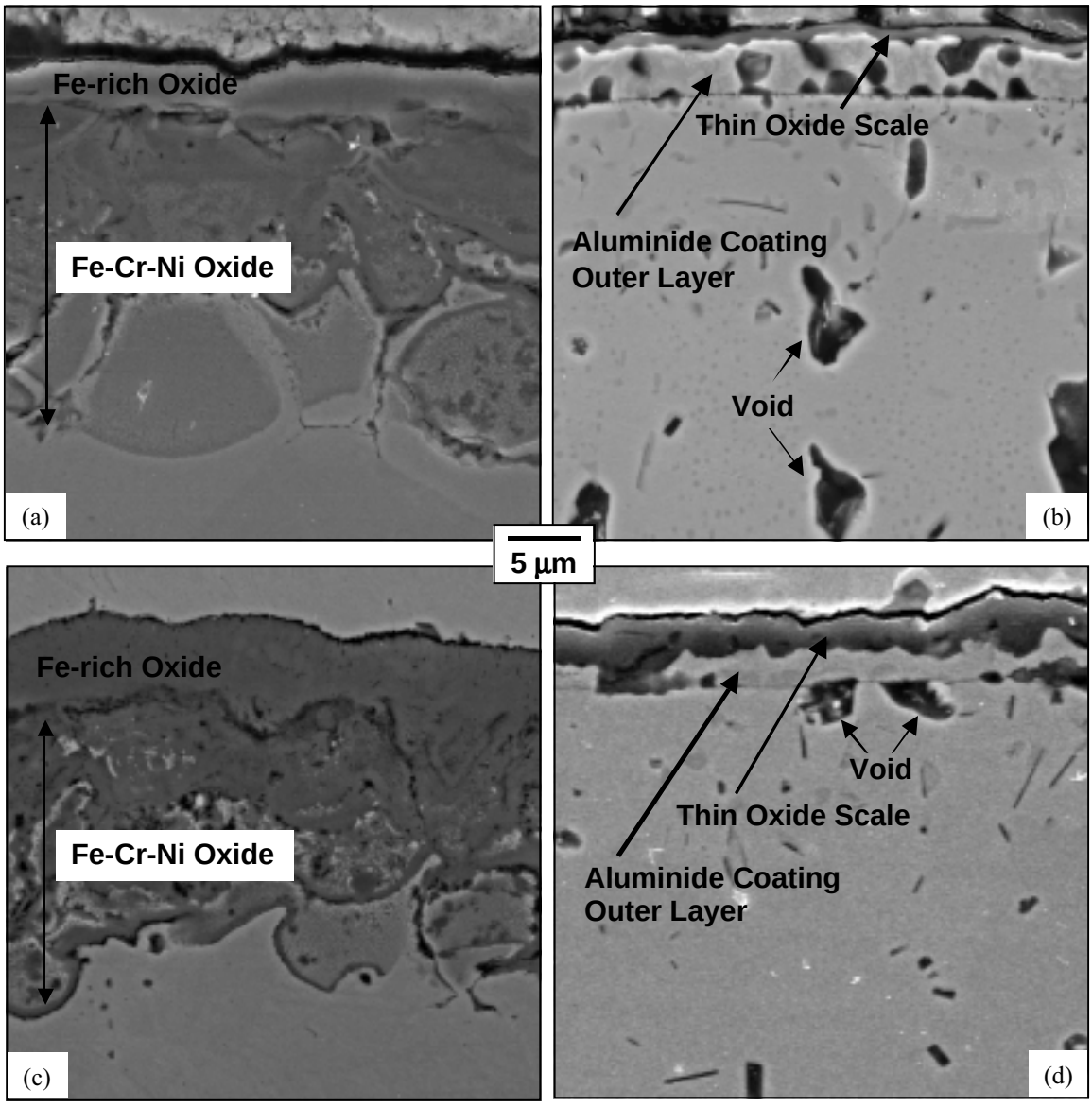

Fig. 9. SEM secondary electron images of cross-sections of 304L with and without aluminide coatings after thermal cycling in air + 10vol.% H_2O: (a) without a coating after 200 1-h cycles at 700°C; (b) with a coating after 1000 cycles at 700°C; (c) without a coating after 200 cycles at 800°C; (d) with a coating after 500 cycles at 800°C.

In addition, voids were found in both coated Fe-9Cr-1Mo and 304L after thermal cycling, as shown in Figures 7(b), 7(d), 9(b), and 9(d). These voids were present in the as-deposited specimens and more voids seemed to exist in the coated 304L, particularly along the interface of the coating outer layer and inner layer. Formation of a thin oxide scale was observed around some of the voids near the interface of coated 304L, Figure 11, indicating some attack in this area during exposure.

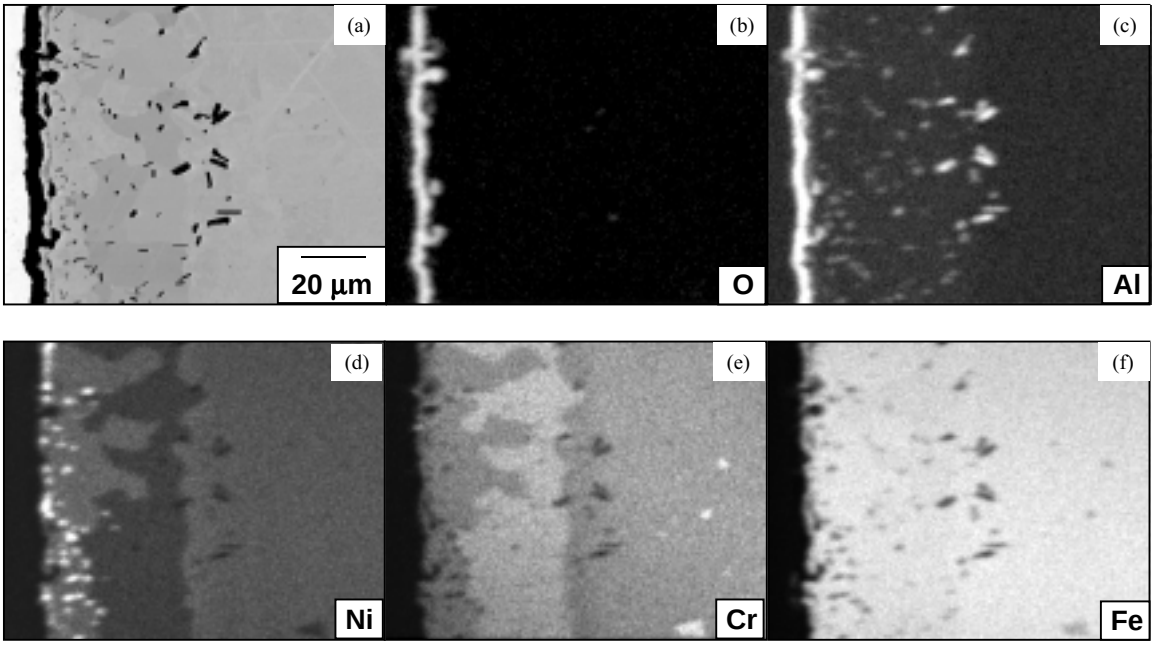

Fig. 10. (a) EPMA back-scattered electron cross-sectional image of coated 304L after 500 1-h cycles at 800°C in air + 10vol.% H_2O. X-ray maps of the same region showing (b) O, (c) Al, (d) Ni, (e) Cr, and (f) Fe.

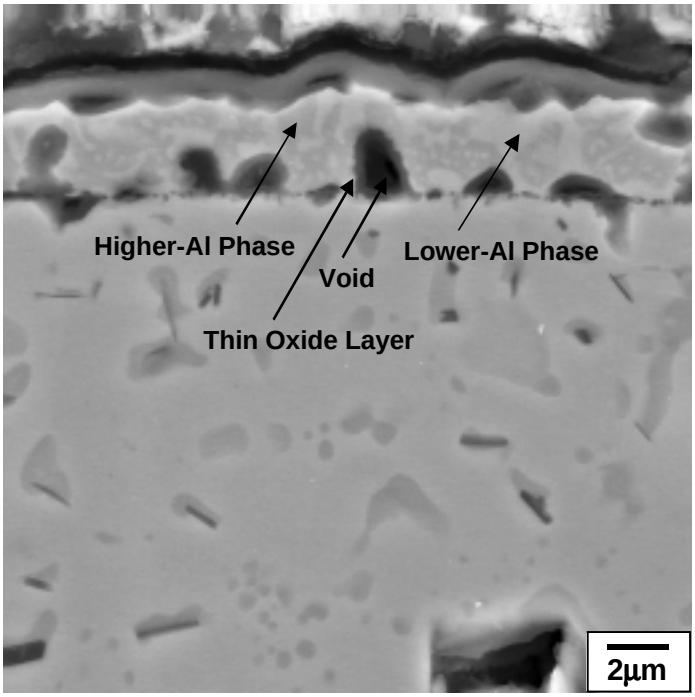

Fig. 11. SEM secondary electron image showing the formation of a two-phase microstructure in the coating on 304L after thermal cycling at 700°C in air + 10vol.%H_2O.

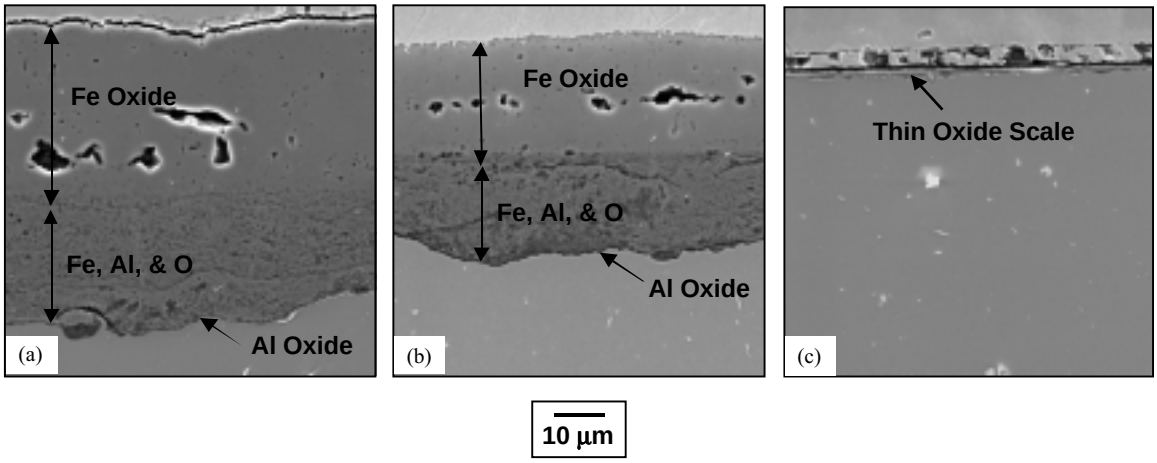

Fig. 12. SEM secondary electron images of cross-sections of cast Fe-Al+Hf with various Al contents after 800 1-h cycles at 700°C in air + 10vol.% H_2O: (a) 13at% Al; (b) 15at% Al; (c) 20at% Al.

Cast Fe-Al alloys with 13-20%Al + Hf were cycled under the same conditions as the coating specimens. As an example, Figure 12 compares the cross-sections after 800 1-h cycles at 700°C in air + 10vol.% H_2O. Both Fe-13%Al and Fe-15%Al formed very thick oxide scales, approximately 55-60µm and 40-45µm, respectively. The oxide scales consisted of three layers: an outer Fe_2O_3 layer, a thin inner layer of Al oxide and a mixed Fe-Al oxide layer in between. However, only a thin Al oxide (<2µm) scale was formed on Fe-20%Al. This result was in a good agreement with the mass change curve in Figure 2(a). These results also suggested that the thin Al-rich outer layer in the coating is important in forming a protective Al_2O_3 scale on coating specimens. However, these binary alloys do not contain Cr as is found in the coatings. The addition of Cr assists in the formation of a protective alumina layer [13] by a third element effect.[14]

1.1.4. Discussion

It is well known that the presence of water vapor may significantly affect the high-temperature oxidation behavior of some metals and alloys. The oxidation resistance of ferritic and austenitic steels is based on their ability to form a protective chromia or Cr-rich external scale. The minimum Cr content required in ferritic alloys is about 13-14wt.% over the temperature range 800-1200°C in O_2-rich atmospheres.[15] Below this Cr level, the growth of an external Fe_2O_3 layer, surmounting a chromia subscale, or the formation of a mixed oxide $(Fe,Cr)_2O_3$, has been observed.[1, 16] For austenitic Fe-Cr-Ni alloys, on the other hand, a continuous chromia scale is not as easily developed in air as on the corresponding ferritic Fe-Cr alloys. This is likely due to the lower Cr diffusivity in the austenitic metallic substrate.[17, 18]

A further problem is that chromia-forming alloys which exhibit protective behavior in dry oxygen can show accelerated attack in the presence of water vapor. A number of mechanisms [19-22] have been proposed to explain the water vapor effect. These include formation and evaporation of volatile Cr-oxihydroxides or Fe-hydroxides,

enhanced surface reaction kinetics, proton defects in the oxide lattice, and formation of oxygen bridges by H_2O/H_2 mixtures in oxide pores. While the exact mechanism has not been clarified, in general, most technologically useful steels oxidize faster in humid air or combustion gases containing water vapor than in the corresponding dry gases. It has been observed that the destruction of the protective scale by water vapor depends on the H_2O content as well as the H_2O/O_2 ratio.[20]

It is well known that Al additions to iron decrease the oxidation rate in dry air.[16] This is due primarily to the formation of a protective $FeAl_2O_4$ spinel layer; development of an alumina scale occurs when the Al content is at least ~12-19at.% (6-10wt.%), which results in considerable further decreases in the oxidation rate.[4, 16, 23-24] However, unlike chromia-formers, there seems to have been few detailed studies of the effect of water vapor on the oxidation behavior of alumina-forming alloys, most likely because Al_2O_3 apparently is less affected by H_2O.[25-27] Kvernes et al. [28] studied Fe-13Cr-xAl (wt.%) alloys containing up to 4.5Al in the temperature range of 680-980°C in 0.03-2.3vol.% H_2O, and found that higher critical levels of Al were required for good oxidation resistance as the test temperature increased. Buscail et al. [29] concluded that once a continuous Al_2O_3 scale was formed, the oxidation was not significantly dependent on the water vapor content in air. Other reported studies have focused on the effect of water vapor on the oxidation performance of Ni-base superalloys and aluminide coatings on these alloys.[30-34] The results suggest that water vapor may play a role in scale adhesion for thicker alumina scales grown at higher temperatures of 1100-1200°C. However, in the lower temperature regime, such as the testing conditions in the present study, thin scales are less likely to be affected by these issues.

The present work provided a detailed comparison of oxidation behaviors of CVD aluminized and uncoated chromia-forming steels in a water vapor environment in the temperature range of 700-800°C. Results based on specimen mass changes and microstructural characterization indicated that a very thin aluminide coating (<5μm) on both ferritic and austenitic alloys significantly improved the resistance of these alloys to water vapor attack. The oxidation products were transformed from thick duplex scales with an Fe-rich outer layer and Cr-Fe (or Cr-Ni-Fe) mixed inner layer to a continuous, thin aluminum oxide. The alumina scale survived 1000 1-h cycles at 700°C and 500 cycles at 800°C without any significant scale spallation. Cyclic oxidation tests on cast Fe-Al alloys with 13-20%Al suggested that a critical Al content is necessary to form a protective aluminum oxide without forming a thick Fe-rich oxide. This critical level is dependent on the Cr content in the coating.[7]

The cross-sections of Fe-9Cr-1Mo without a coating after exposure in air + 10vol.% H_2O at the present testing temperatures were similar to those observed by Nickel et al. [20] However, a duplex oxide scale was observed in the present study, while porous scales consisting of three layers [Fe_2O_3 (outer), Fe_3O_4 (middle) and $(Fe,Cr)_3O_4$ (inner)] were reported in their 100h isothermal oxidation test at 650°C in N_2-1%O_2-2%H_2O. In that study, a protective scale was formed on bare Fe-9Cr-1Mo at 800°C irrespective of the H_2O content (2-4vol.%) in the gas, whereas, with a higher water content (10vol.% H_2O) in the present study, significant attack was observed on uncoated Fe-9Cr-1Mo

during 1-h cycles and even during short-term (24h) test at 800°C.[35] The results of these studies suggest that there may be a critical level of water vapor between 4 and 10vol.%H_2O at 800°C for uncoated Fe-9Cr-1Mo, above which the transformation from protective to accelerated attack occurs. However, other factors such as alloy grain size may also explain the difference.[36]

The results from this study support other observations that accelerated attack by water vapor is a significant problem for some ferritic and austenitic alloys. Coatings which enable the formation of an alumina scale are able to protect the substrate alloy under these conditions. These tests simulated exhaust gas environments. Further work is necessary to determine if these coatings will be effective in steam environments.

1.1.5. Conclusions

Fe-9Cr-1Mo ferritic and type 304L austenitic stainless steel are known to have reasonably good oxidation resistance at 700-800°C in dry air; but, accelerated attack has been observed in the presence of water vapor. The present study clearly demonstrates that a thin CVD aluminide coating (~5μm) can substantially improve the short-term (1000 cycles at 700°C and 500 cycles at 800°C) resistance of these alloys to water vapor attack. Protective thin alumina scales have been formed on the aluminized specimens, in contrast to thick duplex oxide scales on uncoated alloys. Thus, aluminide coatings which facilitate the formation of protective alumina scales appear to be an attractive option for chromia-forming steel alloys in high-temperature exhaust gas environments.

1.2. The Interdiffusion Behavior between Iron Aluminide Coatings and Steel Substrates

1.2.1. Introduction

Increasing the temperature capabilities of ferritic and austenitic alloys for advanced power generation applications has been of ongoing interest for many years due to potential gains in energy efficiency and concomitant decreases in emissions. These classes of alloys generally owe their oxidation resistance to the formation of Cr-containing oxides which, especially for the ferritic steels, become less protective at higher temperatures and in steam or exhaust environments so that protective coatings will have to be considered.[1, 2] Iron aluminides are well known to have excellent oxidation and sulfidation resistance due to the formation of an external, protective alumina scale.[3-6] Thus, an aluminide coating could be a good candidate for improving the oxidation/corrosion resistance of ferritic and austenitic steels provided that it can be applied with the desired composition and microstructure and be mechanically sound (that is, minimal cracking and adherent to the substrate).

Two lifetime issues of particular concern for application of iron aluminide coatings are (1) the loss of Al from the coating into the substrate alloys which do not contain any Al, and (2) possible compatibility problems between Fe-Al coatings and steel substrates which can have substantially different CTE.[7] In the present work, the interdiffusion behavior between CVD aluminide coatings and ferritic and austenitic substrates is being studied for times up to 10,000h in the temperature range of 500-800ºC. Representative commercial ferritic (Fe-9Cr-1Mo) and austenitic (type 304L stainless steel) alloys were used as the substrate materials. Coatings were synthesized using a laboratory-scale CVD reactor in order to more rigorously control the coating process in terms of composition, purity and microstructure. The interdiffusion between the coating and substrate alloys was simulated using a computer model COSIM (Coating Oxidation and Substrate Interdiffusion Model), which was originally developed for MCrAlY overlay coatings by Nesbitt.[37] Another model developed by Heckel et al. in the 70's concerning the kinetics of phase layer growth during the aluminization of iron and during subsequent diffusion treatment also was used to calculate the surface Al concentration and the coating thickness after the diffusion tests.[38] Both COSIM and Heckel's models were used to predict lifetime of the present aluminide coating systems based on a concentration dependent failure criterion, i.e., lifetime is defined as the time for the Al content at the coating surface to drop to a critical level. While the complexity of the transport processes from experimental and theoretical studies of interdiffusion in aluminide coatings on Ni-based superalloys has been recognized,[39-41] very limited research could be found on interdiffusion behavior between aluminide coatings and Fe-based alloys.[42, 43] The results from the present study could therefore provide data and insight needed as part of the process of developing a lifetime model based on coating failure criteria. It is expected that the understanding of these critical issues could readily be applied to diffusion aluminide coatings produced by other aluminizing techniques, such as commercial pack coatings.

1.2.2. Experimental Procedures

The substrates used in this study were commercial ferritic (Fe-9Cr-1Mo) and type 304L (Fe-18Cr-9Ni nominally) austenitic stainless steels. These particular alloys are considered to be representative of the basic compositions of the two alloy classes of interest. Prior to coating experiments, the substrate surface was polished to a 0.3mm alumina finish and ultrasonically cleaned in acetone and methanol. The iron aluminide coatings were made in a laboratory CVD reactor at ORNL, and details of the coating fabrication process have been reported elsewhere.[9, 44]

The diffusion tests are being conducted on the coated steel specimens contained in crucibles in air for times up to 10,000h in the temperature range of 500-800ºC, as indicated in Table 2. Before and after diffusion tests, selected specimens were examined by XRD and FEM-SEM, equipped with EDS. The coatings on specimens for cross-sectional examination were protected by Cu-plating the specimen prior to mounting in epoxy. The composition profiles were measured by EPMA using wavelength dispersive x-ray analysis.

Table 2. The diffusion test conditions.

Coating System	Diffusion Temperature (°C)	Diffusion Time (h)
CVD aluminide coatings on Fe-9Cr-1Mo and 304L	500	10,000*
	600	5,000
		10,000*
	700	2,000
		5,000
		10,000*
	800	2,000

* Still in testing at the present time

The ultimate purpose of the diffusion modeling work was to use the experimental results from the present diffusion tests to predict the iron aluminide coating lifetime. The coating composition profiles were simulated using the finite-difference computer program COSIM,[37, 45] which was originally designed to model one-dimensional, diffusional transport associated with high-temperature oxidation and interdiffusion of overlay-coated substrates. Concentration profiles for up to three elements in the coating and substrate can be predicted after various oxidation exposures. In addition, an earlier mathematic model developed by Heckel et al. (designated as "Heckel's model" hereafter) for aluminide coatings on iron which assumes a constant Al mass during interdiffusion process was used to calculate the coating growth and the change of Al concentration at the coating surface after the diffusion tests.[38] Based on the simulated Al composition

profiles or surface Al concentration, the coating lifetime was calculated by using a critical Al content criterion.

1.2.3. Results and Discussion

1.2.3.1. Diffusion Tests

The as-deposited aluminide coatings on both alloys typically consisted of a relatively thin (20-25µm) Al-rich outer layer and a thicker (150-250µm) inner layer with less Al, as shown in Figure 13. The EPMA composition profiles of the coated specimens before and after the diffusion tests at 600°C for 5,000h are shown in Figure 14; the color plots correspond to the as-deposited compositions, while the black plots are for the specimens after diffusion treatment. Interdiffusion between the CVD aluminide coatings and Fe-9Cr-1Mo and 304L substrates was negligible after 5,000h at 600°C; the surface Al content remained the same as the as-deposited conditions, ~25% (all coating compositions are given in at.% hereafter) in the coating on Fe-9Cr-1Mo (Figure 14a) and ~32% on 304L (Figure 14b), respectively.

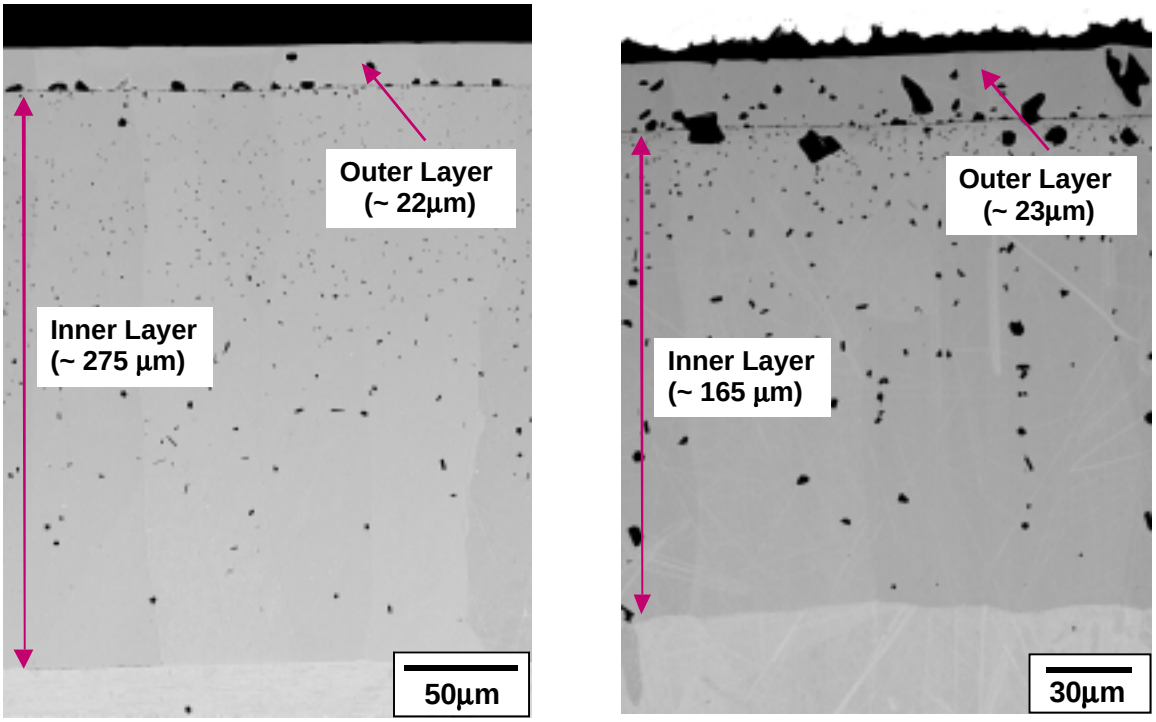

(a) (b)

Fig. 13. EPMA back-scattered electron images of the as-deposited CVD aluminide coating on (a) Fe-9Cr-1Mo and (b) 304L.

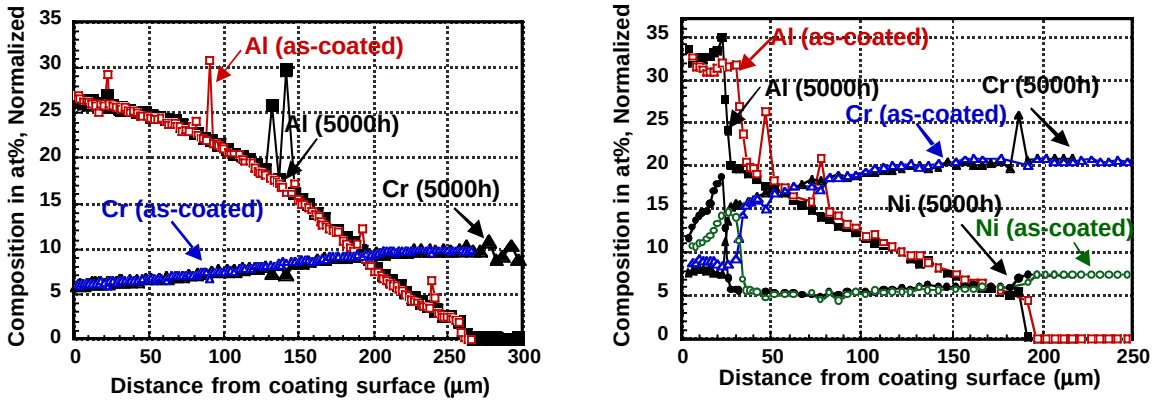

Fig. 14. Composition profiles in the CVD aluminide coatings before and after diffusion at 600°C for 5000h. (a) coatings on Fe-9Cr-1Mo and (b) coatings on 304L.

A decrease of Al at the coating surface was noticed when the diffusion temperature was increased to 700°C. As an example, the surface Al content decreased from 26% to 23% in the coating on Fe-9Cr-1Mo after 2,000h at 700°C, and further dropped to 20% after 5,000h, as shown in Figure 15a. A decrease from 34% Al to 25% was found near the coating surface on 304L after 2000h, Figure 15b.

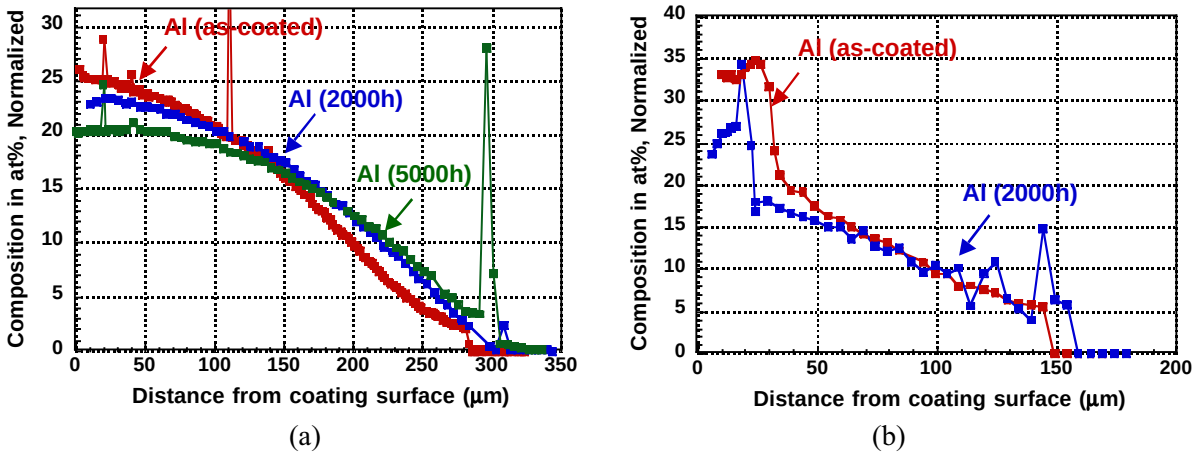

Fig. 15. Composition profiles of Al in the CVD aluminide coatings before and after diffusion at 700°C. (a) coatings on Fe-9Cr-1Mo and (b) coatings on 304L.

The interdiffusion was much greater at 800ºC, as indicated in Figure 16, where color and black plots correspond to before and after diffusion testing for 2,000h, respectively. A significant decrease of Al from 25% to 12% was observed in the coating on Fe-9Cr-1Mo after 2,000h, Figure 16a. The total coating thickness (outer layer + inner layer) was increased from ~275μm to ~500μm. The decrease of Al in the coating on 304L from ~32% to 15-20% led to the formation of a two-phase microstructure in the coating outer layer, as shown in Figure 17, which also was reflected in the fluctuation in the composition profiles, Figure 16b. The EPMA results indicated that the darker phase

contained more Al and Ni (40Al-40Ni-17Fe-3Cr), whereas the lighter phase was depleted in Al but rich in Fe (9Al-4Ni-73Fe-14Cr).

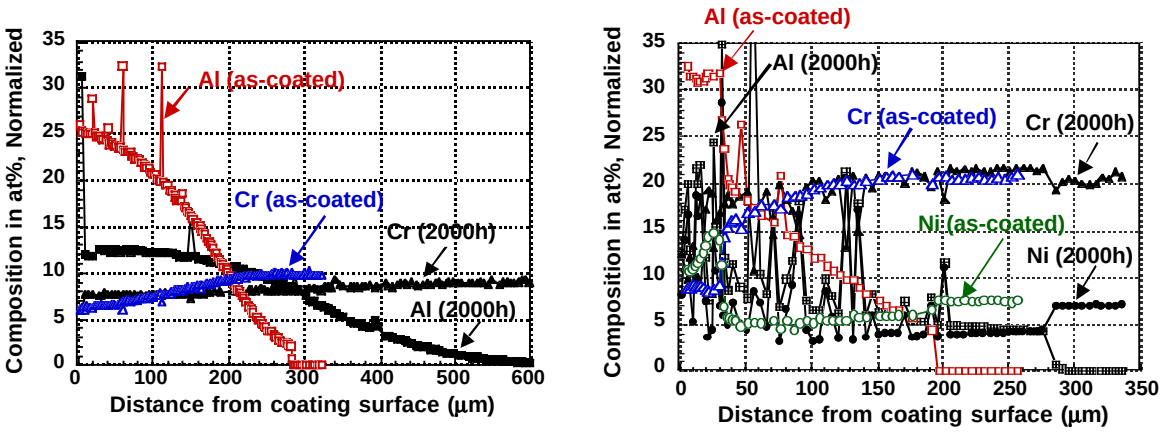

(a) (b)

Fig. 16. Composition profiles in the CVD aluminide coatings before and after diffusion at 800°C for 2,000h. (a) coatings on Fe-9Cr-1Mo and (b) coatings on 304L.

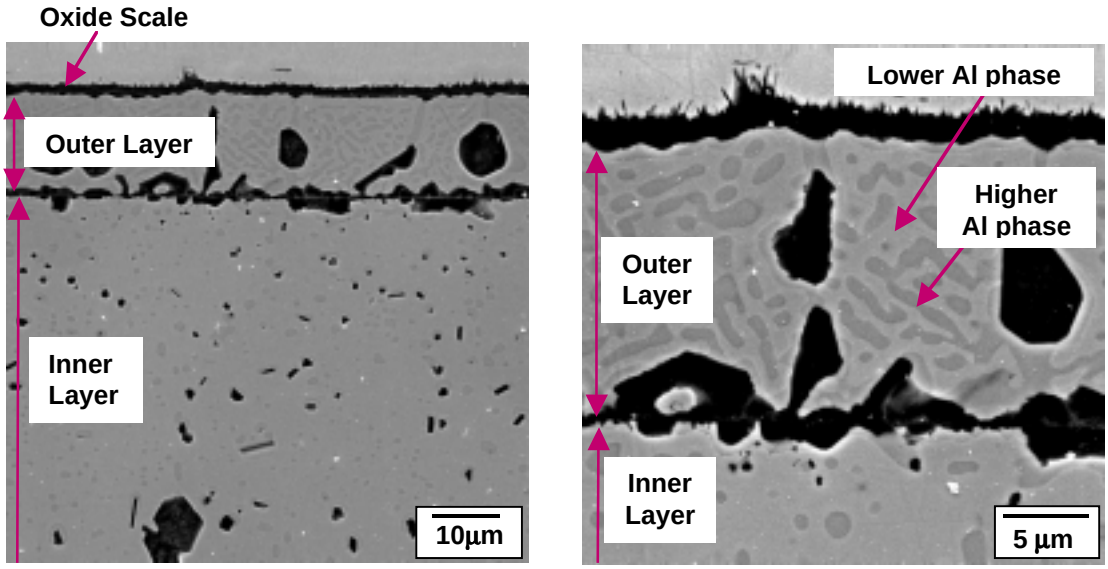

(a) (b)

Fig. 17. (a) EPMA back-scattered electron image showing the two-phase microstructure in the CVD aluminide coating on 304L after diffusion test for 2,000h at 800°C, and (b) higher magnification of the outer layer.

1.2.3.2. Diffusion Modeling

The present diffusion modeling work focused on 700°C, which is a more realistic application temperature for these substrate alloys. The COSIM program incorporates

both the loss of Al at the coating surface due to oxidation and the loss of Al from the coating into the substrate due to interdiffusion.[37] The loss of Al at the coating surface is considered by using a previously-developed oxide growth and spalling model COSP.[46,47] Even though the present diffusion tests were carried out in air, the amount of Al consumed from the coating outer layer by forming the thin oxide layer (~2μm) is relatively small, < 5%, as compared to the Al lost by back diffusion.

In the COSIM, the interdiffusion flux is calculated according to Fick's laws in a ternary system, which includes the diffusional interactions among the components, as shown below:[48]

$$J_j = -D_{j,j}\frac{\partial C_j}{\partial X} - D_{j,k}\frac{\partial C_k}{\partial X} \qquad \text{Fick's 1st Law} \qquad (1)$$

and

$$\frac{\partial C_j}{\partial t} = \frac{\partial\left[D_{j,j}\left(\frac{\partial C_j}{\partial X}\right)\right]}{\partial X} + \frac{\partial\left[D_{j,k}\left(\frac{\partial C_k}{\partial X}\right)\right]}{\partial X} \qquad \text{Fick's 2nd Law} \qquad (2)$$

where J_j and C_j refer to the flux and concentration of component j, $D_{j,j}$ and $D_{j,k}$ refer to the four ternary interdiffusion coefficients, and X and t refer to distance and time, respectively.

As indicated in Equations (1) and (2), the diffusion in a ternary system requires four concentration-dependent interdiffusion coefficients, two main and two cross-coefficients. Two independent diffusion couples with a common composition in the diffusion are usually needed to determine these coefficients.[49] Various methods have been reported in the open literature to calculate ternary interdiffusion coefficients.[50-52] In the original COSIM program, ternary cross terms and concentration-dependent diffusion coefficients were taken into account, such as for the ternary Ni-Cr-Al system at 1100°C.[37] However, no such information with regard to the composition-dependent diffusion coefficients is available for the Fe-Cr-Al or Fe-Ni-Cr system which is needed for the analysis of the present iron aluminide coating systems. The earlier published data has indicated that the interdiffusion coefficient in the Fe-Al binary system is strongly dependent upon the composition, e.g. at 800°C the interdiffusion coefficient increases almost one order in magnitude when the Al concentration increases from 10% to 23%.[53,54] Also, in contrast to MCrAlY overlay coatings which exhibit a constant as-deposited composition throughout the coating thickness, the diffusion aluminide coatings start with a composition gradient, as shown in Figure 14. Because of the above two factors, some modifications were made to the COSIM program in order to apply it to the iron aluminide coatings on steel alloys. The procedure is described below in detail for the aluminized Fe-9Cr-1Mo coating system only, which can be directly applied to the coating system on 304L. Basically, two different approaches were used, and the input diffusion coefficients are given in Table 3. In Approach 1, a binary Fe-Al system was by neglecting the role of Cr in diffusion) and both concentration-dependent and independent diffusivities were used. In Approach 2, a ternary system Fe-Cr-Al with its interdiffusion coefficients (including two main- and two cross-terms) was considered; here, only the concentration-independent diffusion coefficients were used due to lack of data. In both

approaches, an additional step was included to obtain the composition profiles of as-deposited coatings by using the diffusion coefficients at the CVD aluminizing temperature 1050°C (Step I). For Step I, the dependence of diffusivities on concentration did not seem to significantly affect the composition profiles, thus, concentration-independent diffusivities were used to simplify the calculation. For the binary Fe-Al system, the interdiffusion coefficient at 1050°C was obtained directly from Akuezue and Whittle.[42] For the ternary Fe-Cr-Al system, the diffusion coefficients were adapted from Akuezue and Stringer [55] ($C_{Fe} = 100 - C_{Al} - C_{Cr}$), which were given at 900°C, and the diffusivities at other temperatures were estimated based on the activation energy from diffusion of the Fe-Al binary system. Step II considered the diffusion process at 700°C. For the binary system, both concentration-dependent and independent diffusivities were used for this step, which were derived from the plots of the interdiffusion coefficient vs. Al concentration.[42] For the Fe-Cr-Al ternary system, the diffusion coefficients at 22% Al were used in the simulation, which was close to the Al concentration in the present coating system. The concentration-independent diffusivity in the binary Fe-Al system was chosen at the same Al content (22%) for comparison purpose; the binary interdiffusion coefficient used in the present study at 700°C (3.05×10^{-12} cm^2/s) was very close to the value derived by the activation energy reported by Sivakumar and Rao.[56] The composition profiles of Al calculated by the two approaches for the as-deposited aluminide coatings on Fe-9Cr-1Mo, and after 2,000h and 5,000h diffusion tests are shown in Figures 18a-c. The Al concentration at the coating surface and the coating thickness after the diffusion tests are summarized in Table 3. As indicated in Figures 18a, the simulated as-deposited Al profiles by assuming a binary or a ternary system are nearly identical to each other, and very close to the experimental results. However, after 2000h and 5000h of diffusion, the composition profiles calculated by using the concentration-dependent diffusivities of the binary system fit the best with the experimentally measured profiles, even though the role of Cr was not taken into account. This could be explained by relatively small difference of the Cr content in the coating (6-10%) and in the Fe-9Cr-1Mo substrate (10%).

Heckel's model for diffusion of aluminide coatings on iron only applies to the condition where the phases grow during the diffusion process parabolically.[38] The model assumes that if Al neither enters nor leaves the surface during the diffusion treatment, the mass of Al in the material remains constant. In the present study the very small amount of Al consumed in forming the thin oxide scale can be ignored as compared to the Al consumed by interdiffusion. The amount of Al introduced to the coating system during the aluminizing process is taken to be the area underneath the as-deposited Al concentration profile. The phase layer growth rates should be proportional to the reciprocal of the layer thickness if a parabolic behavior applies, and during the diffusion test,[38]

$$X^2 - X_0^2 = 2K_p t \qquad (3)$$

where, X_0 and X are the coating thicknesses before and after diffusion tests, K_p is the parabolic growth constant, and t is the diffusion time. The K_p can be calculated from the measured composition profiles after short-term diffusion testing, e.g. 2,000h, which can then be applied to longer-term diffusion process, such as 5,000h and 10,000h. For diffusion between the iron aluminide coating and Fe-9Cr-1Mo at 700°C, X_0 and X can be

read from the composition profiles, e.g., X_0 = 285μm and X = 310μm at t = 2,000h, and K_p was calculated as 1.033 x 10^{-3} $\mu m^2/s$.

Table 3. Comparison of the calculated surface Al concentration and coating thickness for aluminide coating on Fe-9Cr-1Mo after diffusion test at 700°C by using COSIM and Heckel's model.

<table>
<tr><td colspan="3" rowspan="3"></td><td colspan="3">COSIM</td><td>Heckel's Model</td><td>Experimental results</td></tr>
<tr><td colspan="2">Binary Fe-Al (Approach 1)</td><td>Ternary Fe-Al-Cr (Approach 2)</td><td rowspan="2"></td><td rowspan="2"></td></tr>
<tr><td></td><td></td><td>Composition-independent D</td></tr>
<tr><td rowspan="3">Input</td><td colspan="2">Step I: aluminizing process (cm^2/s)</td><td colspan="2">Composition-independent D:
D(I) = 3.87 x 10^{-9}
at C_{Al} = 26%</td><td>$D_{AlAl}(I)$ = 2.24 x 10^{-9}
$D_{AlCr}(I)$ = -1.03 x 10^{-9}
$D_{CrAl}(I)$ = -2.24 x 10^{-10}
$D_{CrCr}(I)$ = 8.30 x 10^{-10}
at C_{Al} = 27%
C_{Cr} = 11%</td><td rowspan="3">X_0 = 285μm
X = 310μm
t = 2000h</td><td rowspan="3"></td></tr>
<tr><td colspan="2" rowspan="2">Step II: diffusion test (cm^2/s)</td><td>Composition-dependent D</td><td>Composition-independent D</td><td rowspan="2">$D_{AlAl}(II)$ = 2.45 x 10^{-12}
$D_{AlCr}(II)$ = -9.48 x 10^{-13}
$D_{CrAl}(II)$ = -4.36 x 10^{-13}
$D_{CrCr}(II)$ = 5.03 x 10^{-13}
at C_{Al} = 24%
C_{Cr} = 12%</td></tr>
<tr><td>D(II) = (3.96-29.04C_{Al} + 669.73 C_{Al}^2) x 10^{-13}</td><td>D(II) = 3.05 x 10^{-12} at C_{Al} = 22.5%</td></tr>
<tr><td rowspan="4">Output</td><td rowspan="2">Al at coating surface (at%)</td><td>2000h</td><td>22.6</td><td>22.6</td><td>22.6</td><td>23.9</td><td>23.1</td></tr>
<tr><td>5000h</td><td>20.8</td><td>20.0</td><td>20.4</td><td>21.5</td><td>20.7</td></tr>
<tr><td rowspan="2">Coating thickness (μm)</td><td>2000h</td><td>320</td><td>360</td><td>353</td><td>—</td><td>310</td></tr>
<tr><td>5000h</td><td>330</td><td>415</td><td>402</td><td>344</td><td>336</td></tr>
</table>

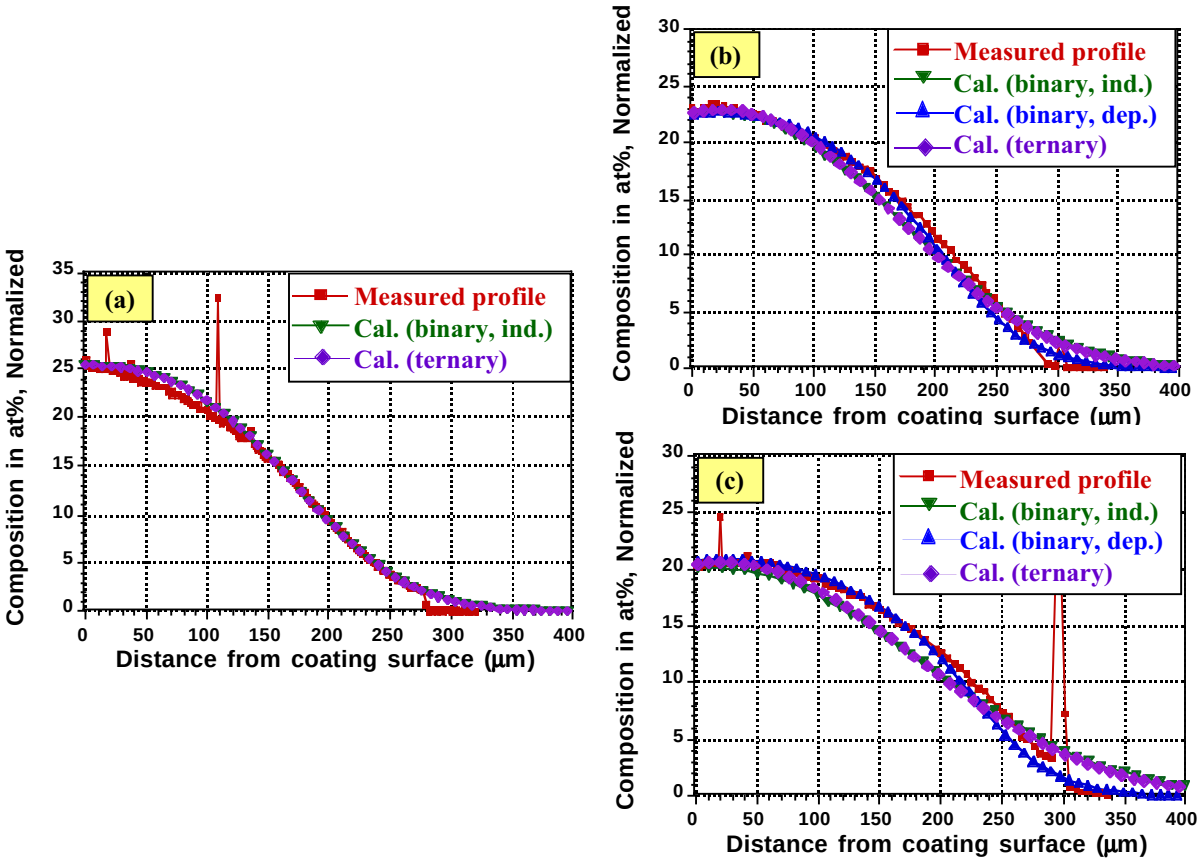

Fig. 18. Comparison Al profiles in aluminide coatings on Fe-9Cr-1Mo between experimentally measured by EMPA and calculated by using COSIM. (a) as-deposited coatings, (b) after 2,000h, and (c) after 5,000h at 700°C; where Cal. (binary, ind.), Cal. (binary, dep.), and Cal. (ternary) designate the calculated profiles by assuming a binary system with concentration-independent diffusivities, a binary system with concentration-dependent diffusivities, and a ternary system, respectively.

The surface Al concentration after the diffusion test may be approximated as [38]

$$C_s \approx \frac{2M}{X} \qquad (4)$$

where, M is the area underneath the as-deposited Al concentration profile which approximates a linear concentration gradient, and C_s is the Al concentration at the coating surface after diffusion.

The coating thickness after 5000h diffusion was estimated by using the K_p calculated from Eq. (3). The Al concentration at the coating surface after 2,000h and 5,000h diffusion was calculated according to Eq. (4). These results are listed in Table 3, and compared with the values obtained by the COSIM and the experimental results. Table 3 indicates that the Al concentration at the coating surface after 2,000h and 5,000h at 700°C was very close to the experimentally measured value by using either COSIM or Heckel's model. However, closer results were obtained for coating thickness when calculated with Heckel's model or with COSIM if the concentration-dependent diffusion

coefficients were used. When a constant diffusivity (at 23-24% Al) was used, the Al diffusion was overestimated since it did not consider the reduction of diffusivity with decreasing in Al (when Al < 26%),[42, 53] and the calculation resulted in a faster coating growth.

However, the situation was more complicated when modeling diffusion in the aluminide coatings on 304L as the coatings contained four major components, Fe, Cr, Al, and Ni.[57] In addition to the binary Fe-Al system (Approach 1), two ternary systems, Fe-Cr-Al ($C_{Fe} = 100 - C_{Al} - C_{Cr}$) and Fe-Ni-Al ($C_{Fe} = 100 - C_{Al} - C_{Ni}$), were used to approximate the multi-component diffusion in Approach 2, and the results are given in Table 4. It has been recognized that a local phase transformation from the austenite to ferrite could be triggered as the Al diffuses into the substrate which has a FCC structure at the diffusion test temperature.[11] The Al diffusion rate in the more open BCC ferrite is about two orders of magnitude higher than that in the tightly packed FCC austenite.[11] Thus, the diffusion induced phase transformation to ferrite in turn helps the Al diffusion. The diffusivity at ~22% Al was used in the Fe-Cr-Al system,[55] while the diffusivity at ~12% Al was used in the Fe-Ni-Al [58] due to limited available data.[59] The Al profiles of aluminide coatings on 304L before and after 2,000h at 700°C calculated by using different approaches are compared with the experimental results, as shown in Figure 19. The surface Al content and the coating thickness after 2,000h were summarized in Table 4. Even though a large difference was noticed between the calculated and measured composition profiles, the surface Al as well as the coating thickness agreed relatively well with the experimental results, particularly when a Fe-Al binary system with a concentration-dependent diffusion coefficient was applied, or the Fe-Ni-Al ternary system was used. Heckel's model can not be applied to the coatings on 304L because the thickness of the outer layer decreases with diffusion time, which does not proceed parabolically.[38, 60]

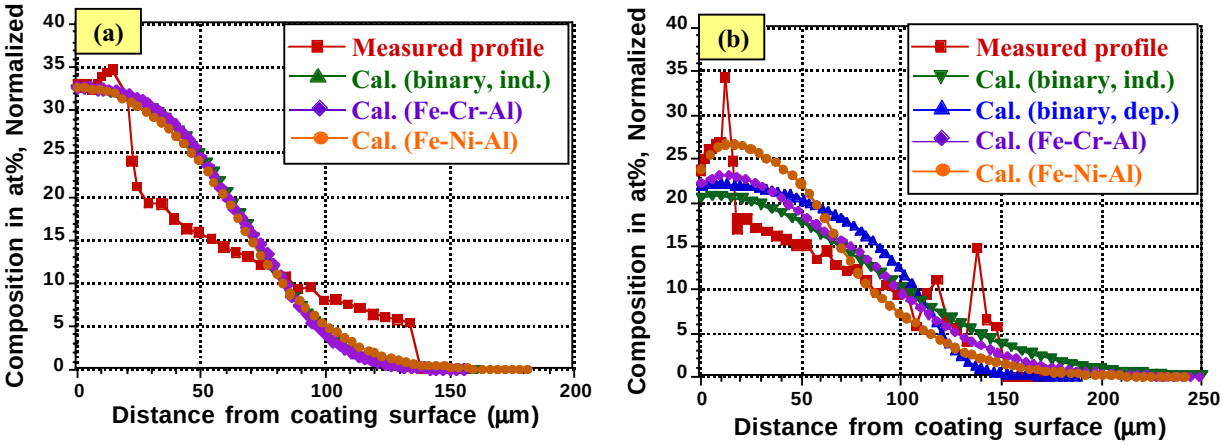

Fig. 19. Comparison Al profiles in aluminide coatings on 304L between experimentally measured by EMPA and calculated by using COSIM. (a) as-deposited coatings and (b) after 2,000h at 700°C; where Cal. (binary, ind.), Cal. (binary, dep.), Cal. (Fe-Cr-Al), and Cal. (Fe-Ni-Al) designate the calculated profiles by assuming a binary system with concentration-independent diffusivities, a binary system with concentration-dependent diffusivities, Fe-Cr-Al and Fe-Ni-Al ternary systems, respectively.

Table 4. Comparison of the calculated surface Al concentration and coating thickness for aluminide coating on 304L after diffusion test at 700°C by using COSIM model.

<table>
<tr><td></td><td></td><td colspan="4">COSIM</td><td>Experimental results</td></tr>
<tr><td></td><td></td><td colspan="2">Binary Fe-Al</td><td>Ternary Fe-Cr-Al</td><td>Ternary Fe-Ni-Al</td><td></td></tr>
<tr><td rowspan="3">Input</td><td>Step I: aluminizing process (cm^2/s)</td><td colspan="2">Composition-independent D: $D(I) = 3.26 \times 10^{-9}$ at $C_{Al} = 24\%$</td><td>$D_{AlAl}(I) = 2.31 \times 10^{-9}$
$D_{AlCr}(I) = -8.93 \times 10^{-10}$
$D_{CrAl}(I) = -4.11 \times 10^{-10}$
$D_{CrCr}(I) = 4.74 \times 10^{-10}$
at $C_{Al} = 24\%$, $C_{Cr} = 12\%$</td><td>$D_{AlAl}(I) = 2.27 \times 10^{-9}$
$D_{AlNi}(I) = -5.95 \times 10^{-10}$
$D_{NiAl}(I) = -4.49 \times 10^{-10}$
$D_{NiNi}(I) = 4.35 \times 10^{-10}$
at $C_{Al} = 14\%$, $C_{Ni} = 7\%$</td><td></td></tr>
<tr><td rowspan="2">Step II: diffusion test (cm^2/s)</td><td>Composition-dependent D</td><td>Composition-independent D</td><td rowspan="2">$D_{AlAl}(II) = 1.63 \times 10^{-12}$
$D_{AlCr}(II) = -1.00 \times 10^{-12}$
$D_{CrAl}(II) = -5.23 \times 10^{-13}$
$D_{CrCr}(II) = 3.83 \times 10^{-13}$
at $C_{Al} = 22\%$, $C_{Cr} = 17\%$</td><td rowspan="2">$D_{AlAl}(II) = 8.77 \times 10^{-13}$
$D_{AlNi}(II) = -6.17 \times 10^{-13}$
$D_{NiAl}(II) = -5.71 \times 10^{-13}$
$D_{NiNi}(II) = 4.44 \times 10^{-13}$
at $C_{Al} = 12\%$, $C_{Ni} = 10\%$</td><td></td></tr>
<tr><td>$D(II) = (3.96 - 29.04C_{Al} + 669.73\ C_{Al}^2) \times 10^{-13}$</td><td>$D(II) = 2.90 \times 10^{-12}$ at $C_{Al} = 22\%$</td><td></td></tr>
<tr><td rowspan="2">Output</td><td>Al at coating surface (at%)</td><td>22.0</td><td>20.6</td><td>22.3</td><td>23.7</td><td>24</td></tr>
<tr><td>Coating thickness (μm)</td><td>143</td><td>206</td><td>184</td><td>169</td><td>154</td></tr>
</table>

1.2.3.3. Coating Lifetime Prediction

COSIM and Heckel's model also were used to predict coating lifetime based on a critical Al concentration failure criterion,[8] which assumes that as the Al in the coating is consumed by surface oxidation and/or back-diffusion into the substrate, there will be a critical Al content, below which the coating is no longer effective in protecting the underlying substrate. Previous studies on cast Fe-based alloys with 13-22% Al and 500 ppma Hf during exposure in wet air at 700°C indicated that 20% Al was necessary for forming protective Al_2O_3 scales.[13] However, as shown in Figure 14 the present

aluminide coatings contained a significant amount of Cr (8-9%) and this Cr addition was expected to improve the oxidation resistance of the coatings.[14, 61] Oxidation tests in wet air at 700°C on cast alloys with 13-15% Al, 2-10% Cr and 500 ppma Hf suggested that the Cr addition had a significant beneficial effect; an alloy with only 13% Al performed as well as the Fe-20% Al+Hf specimen.[13] Thus, when substantial Cr is present in the coating, as is the case for the coatings on Fe-9Cr-1Mo and 304L, the critical Al content appears to be less than 13% Al. According to these oxidation results, three Al contents, 20%, 16%, and 12% were selected as possible critical surface concentration at failure for predicting coating lifetime; the results are given in Table 5.

Table 5. The results of lifetime prediction of coatings on Fe-9Cr-1Mo and 304L at 700°C by COSIM and Heckel's model based on a critical Al concentration failure criterion.

Lifetime (kh)				
Coating on Fe-9Cr-1Mo				
	COSIM			Heckel's Model
	Binary Fe-Al		Ternary Fe-Al-Cr	
Critical Al Concentration at Surface (at%)†	Composition-dependent D	Composition-independent D	Composition-independent D	
20	6.9	5.0	5.6	7.5
16	23.7	11.9	13.6	17.9
12	67.6	25.0	28.9	40.3
Coating on 304L				
	COSIM			
	Binary Fe-Al		Ternary Fe-Al-Cr	Ternary Fe-Ni-Al
Critical Al Concentration at Surface (at%)†	Composition-dependent D	Composition-independent D	Composition-independent D	Composition-independent D
20	3.1	2.2	2.8	5.2
16	7.4	3.9	4.9	12.9
12	17.9	7.1	8.9	34.0

† Assume that the coating failure will occur when the Al concentration at the coating surface drops to these critical values

When a binary system was assumed, the predicted coating life was much shorter if the effect of the Al content on the diffusion coefficients were not taken into account. The difference was more significant when a lower surface Al critical content was used as the failure criteria. This was as explained earlier, i.e., the predicted coating life based on the Al diffusivity at ~22% was underestimated since the actual diffusivity decreases with depleting of Al in the coating layer. For coatings on 304L, the coating life predicted by

the Fe-Ni-Al system was much higher because the diffusivity at a lower Al level (~12%) was used.

These calculations suggest that with the present Al content and coating thickness on Fe-9Cr-1Mo, the coating lifetime corresponding to the critical surface concentration of 12% Al seems satisfactory for the goal of 40 kh lifetime in power generation applications. Further increasing the Al content and/or coating thickness of as-deposited aluminide coatings could certainly maintain the Al level required to form protective scales at the coating surface for longer period of time. However, CTE mismatch between coating and the substrate is more likely to become a concern for thicker coatings with higher Al contents, which could cause cracking or deformation and therefore reduce coating life.[62]

The major advantage of the COSIM program is that it considers both the loss of Al from the coating into the substrate during interdiffusion and the loss of Al at the coating surface during oxidation. The limitation for application is mainly due to lack of published data for ternary diffusion coefficients, particularly when they are a strong function of concentration. The Heckel's model, on the other hand, has the simplicity when applied to those coating layers whose thickness increases with diffusion time, such as the aluminide coating on Fe-9Cr-1Mo in the present study. If the Al concentration profiles shows a nearly linear gradient, a short-term diffusion experiment can be conducted to calculate the parabolic kinetics constant K_p, which can then be used to predict the surface Al concentration after long-term diffusion process. The coating lifetime can be projected if a critical Al content is used as the failure criterion. However, it should be noted that the deviation of the actual concentration profile from a linear gradient could lead to the discrepancy of the predicted surface concentration and the experimentally determined one.

1.2.4. Conclusions

The interdiffusion behavior between CVD aluminide coatings and ferritic and austenitic substrates is being studied for times up to 10,000h in the temperature range of 500-800°C. The decrease of the Al content at the coating surface was not significant after extended diffusion times (≤ 5,000h) at temperatures ≤ 700°C. Interdiffusion at 800°C led to a greater decrease of Al and the formation of a two-phase microstructure in the outer coating layer on 304L. The aluminide coating composition profiles after diffusion testing at 700°C were simulated using the COSIM computer model. Another mathematic model by Heckel also was used to calculate the Al concentration at the coating surface and the coating thickness after diffusion. Reasonable agreement was obtained between the simulated and experimental composition profiles for coatings on Fe-9Cr-1Mo. Simplification of the quaternary Fe-Ni-Cr-Al to either a binary or ternary system, as well as lack of diffusion data could lead to the discrepancy between the calculated and measured composition profiles of the coating on 304L.

2. Task II. Aluminide Coatings on Ni-based Superalloys

2.1. Martensitic Transformation in CVD NiAl and (Ni,Pt)Al Bond Coatings*

2.1.1. Introduction

State-of-the-art thermal barrier coating (TBC) systems consist of a strain-tolerant Y_2O_3-stabilized-ZrO_2 (YSZ) layer prepared by electron beam-physical vapor deposition (EB-PVD) and a metallic bond coat, such as (Ni,Pt)Al, which provides oxidation protection. The single-phase (Ni,Pt)Al bond coat is typically deposited via a low-activity vapor aluminizing process.[63] Recent work has focused on the oxidation behavior and degradation modes of the (Ni,Pt)Al coating, with regard to TBC failure mechanisms.[64-67] The starting Al concentration (~40at%) in single-phase β-(Ni,Pt)Al is usually lower than that in traditional high-activity simple aluminide coatings.[68] Furthermore, the service temperatures these bond coats are experiencing are usually higher compared to simple NiAl coatings, leading to greater interdiffusion between the coating and substrate alloys even though the Al consumed by scale spallation and re-formation is reduced due to improved scale adhesion with Pt incorporation. Consequently, the current (Ni,Pt)Al bond coat is a Ni-rich β-phase that becomes more Ni-rich after high-temperature exposure. As observed in Ni-rich Ni-Al alloys, when the Al content is less than a critical level, the β phase can undergo a martensitic transformation if cooled at a sufficiently fast rate.[69] This martensitic transformation has been observed in simple NiAl coatings when Al was depleted by interdiffusion and Al_2O_3 scale spallation and re-formation.[70, 71] Although martensitic transformations are not a new phenomenon in Ni-Al alloy systems, there have been very limited investigations of the transformation in today's (Ni,Pt)Al bond coats.[72] On the other hand, surface plastic instability, or "rumpling", has been noticed during cyclic oxidation of both aluminide and platinum aluminide coatings for many years.[73] As martensite reactions are commonly accompanied by volume changes, this could contribute to rumpling of (Ni,Pt)Al bond coats during thermal cycling.[70-71, 74] The martensitic transformation could also enhance other degradation modes by inducing cracks or exposing more surface area to oxidation. The purpose of the present work is to show experimental evidence of martensitic transformations in NiAl and (Ni,Pt)Al coatings on Ni-based superalloys.

2.1.2. Experimental Procedures

The specimens investigated in the present study were from two sources. The isothermal oxidation specimens [75] were single-phase NiAl and (Ni,Pt)Al coatings on a yttrium-free single-crystal Ni-based superalloy René N5'. These specimens were coated via a CVD technique; process details are reported elsewhere.[9, 65] The specimens for cyclic oxidation were (Ni,Pt)Al bond coat discs provided by Howmet Corporation on René N5 with EB-PVD TBC on one side and bond coat only on the other side. Both isothermal and cyclic oxidation tests were performed at 1150°C in dry, flowing O_2 and the specimens were hung on a Pt wire. They were rapidly inserted and removed from the

* Y. Zhang, J. A. Haynes, B. A. Pint, I. G. Wright, and W. Y. Lee, *Surf. Coat. Technol.*, 163-164 (2003) 19.

hot furnace and air-cooled to room temperature, with a cooling rate of approximately 200°C/min. The isothermal oxidation consisted of 100-h exposure at 1150°C. The cyclic oxidation was conducted in an automated furnace rig. Each cycle consisted of a 1-h exposure at 1150°C followed by a 10-min cooling in air.

The phase structures of the as-deposited and oxidized specimens were determined by room temperature XRD using Cu K_α radiation. The oxide scales on isothermal oxidation specimens were carefully removed by polishing and the polished coating surface was re-examined by XRD to reveal the major phases in the coating. The coating surface with oxide scales removed, as well as some coating cross-sections were etched using 5HCl:1HNO_3 etchant to reveal the martensitic structure. The coating microstructure was examined by FEG-SEM. EPMA was used to determine the coating compositions.

2.1.3. Results

The as-deposited CVD NiAl and (Ni,Pt)Al coatings consisted of a layer of single phase β with a B2 CsCl structure with an underlying interdiffusion zone, as reported previously.[65, 75] The average concentrations of alloying elements in the coatings of as-deposited conditions and after isothermal oxidation at 1150°C are given in Table 6. The Al content in both as-coated NiAl and (Ni,Pt)Al coatings was ~40at%.

Table 6. Average concentrations of alloying elements in the outer coating layer of CVD NiAl and (Ni,Pt)Al coatings before and after isothermal oxidation at 1150°C. [75]

Coating	Condition		Ni	Pt	Al	Co	Cr	W	Ta	Re	Mo
NiAl	as-coated (B2 phase)	at%	51.6	—	39.8	5.9	2.6	0.1	0.2	0.1	0.0
		wt%	65.4	—	23.2	7.5	2.9	0.2	0.6	0.2	0.0
	100h ($L1_0$ phase)	at%	57.0	—	31.9	5.7	4.8	0.2	0.2	0.1	0.2
		wt%	68.9	—	17.8	6.9	5.2	0.6	0.8	0.4	0.3
	$\Delta_{comp.}^{*}$		5.4	—	-7.9	-0.2	2.2	0.1	0	0	0.2
(Ni,Pt)Al	as-coated (B2 phase)	at%	46.5	5.5	39.6	4.5	3.6	0.1	0.2	0.0	0.0
		wt%	51.6	20.1	20.3	5.0	3.5	0.2	0.7	0.1	0.0
	100h ($L1_0$ phase)	at%	53.8	3.2	32.1	5.4	4.9	0.1	0.3	0.1	0.1
		wt%	60.1	11.9	16.5	6.1	4.8	0.4	0.9	0.3	0.2
	$\Delta_{comp.}^{*}$		7.3	-2.3	-7.5	0.9	1.3	0	0.1	0.1	0.1

* $\Delta_{comp.}$—Compositional Changes (at%)
= Composition (at%) $_{\text{after oxidation}}$ - Composition (at%) $_{\text{as-coated}}$

After isothermal oxidation at 1150°C for 100h, the remaining β (B2) phase in the coating additive layer transformed to a martensitic phase which has a face-centered tetragonal (f.c.t.) $L1_0$ structure.[69] Figure 20 shows an etched cross-sectional view of the NiAl and (Ni,Pt)Al coatings after isothermal oxidation which indicates the characteristic

striated microstructure of the martensite; this microstructure is very similar to those observed in early simple aluminide coatings.[70] The martensitic structure also was evident from plan view of the etched surface after the Al_2O_3 scale was removed by polishing, as shown in Figure 21. The martensite plates showed different orientations in individual coating grains, Figures 20 and 21. The average compositions of the martensite phase $L1_0$ are given in Table 6. The Al content was reduced from ~40at% to ~32at% after a 100-h exposure at 1150°C. This Al depletion was primarily the result of interdiffusion between the coating and substrate at elevated temperature. A layer of γ′ was observed between the coating and the substrate, as marked in Figure 20.

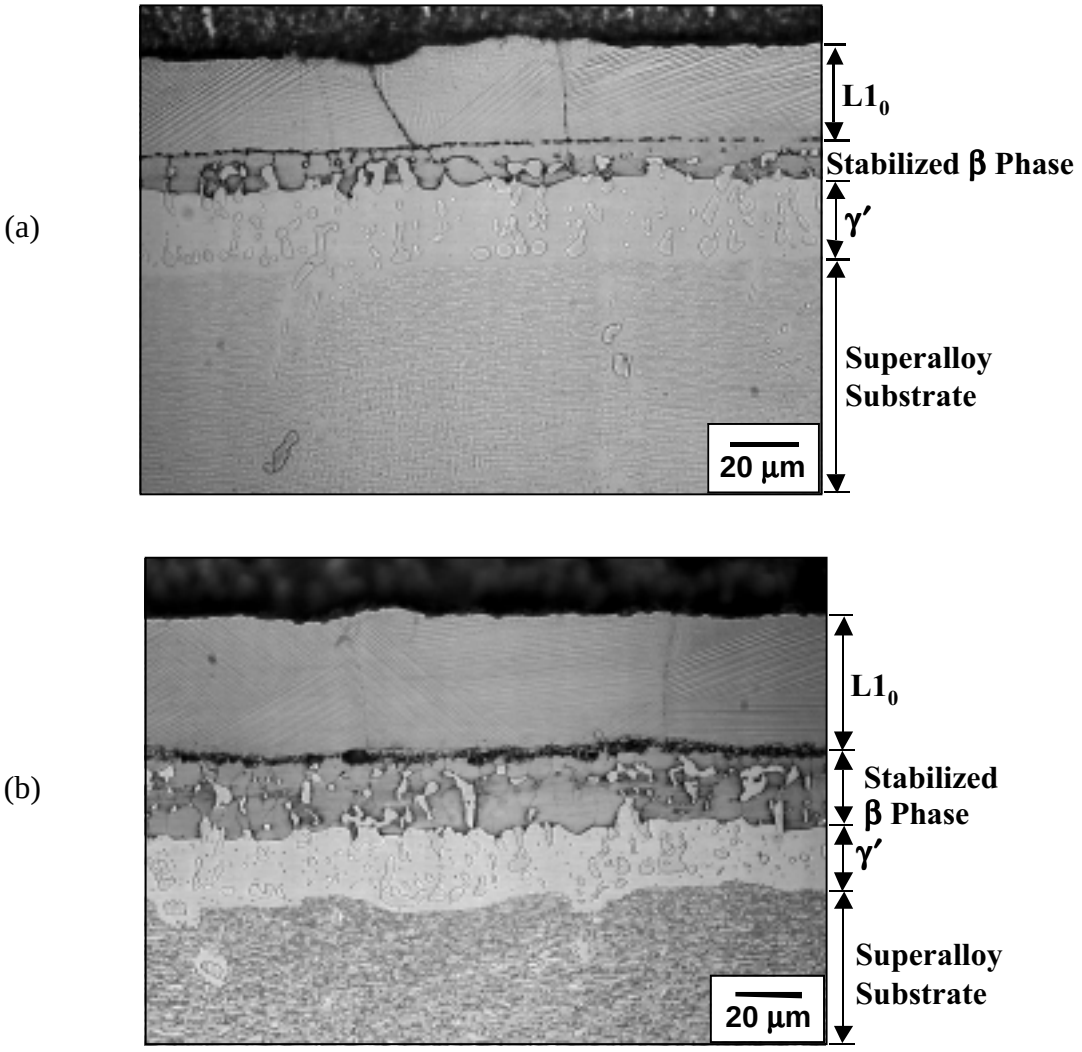

Fig. 20. Etched cross-sectional view of CVD NiAl and (Ni,Pt)Al coatings after isothermal oxidation for 100 hours at 1150°C: (a) NiAl, and (b) (Ni,Pt)Al.

(a)

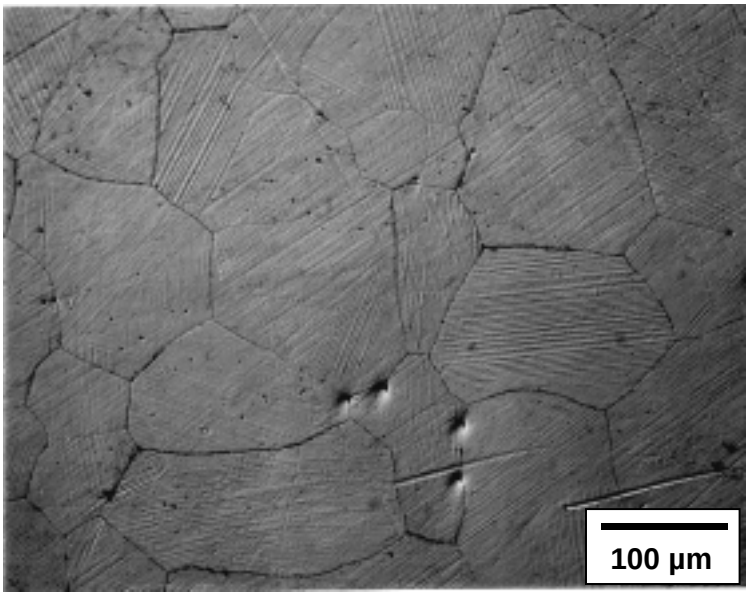

(b)

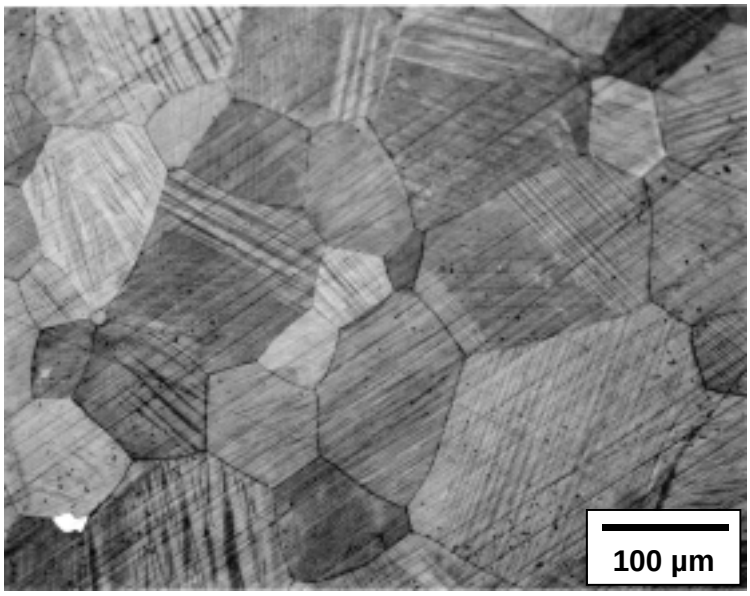

Fig. 21. Etched plan view of CVD NiAl and (Ni,Pt)Al coatings after isothermal oxidation for 100 hours at 1150°C (oxide scales were removed by polishing): (a) NiAl, and (b) (Ni,Pt)Al.

Figure 22 shows the XRD patterns of the NiAl and (Ni,Pt)Al coatings before and after isothermal oxidation. Both as-deposited NiAl and (Ni,Pt)Al coatings were single B2 phase, with preferred orientation, as shown in Figures 22(a) and 22(d).[65] After 100-h oxidation at 1150°C, α-Al_2O_3 was the only oxide formed on the coating surface [~1.2 µm on NiAl and ~1.8 µm on (Ni,Pt)Al, as reported previously.[75] Additional peaks were detected besides α-Al_2O_3 as indicated in Figures 22(b) and 22(e), which were confirmed to be the $L1_0$ phase. After the oxide scale was removed by polishing, the coating layer was found to consist of only the $L1_0$ martensite, Figures 22(c) and 22(f). The lattice

parameter of the B2 phase was calculated as a = 0.2888 nm** for NiAl and a = 0.2889 ± 0.0003 nm for (Ni,Pt)Al. The lattice parameters of the $L1_0$ phase were a = 0.3793 nm and c = 0.3183 nm for the NiAl coating (c/a ≈ 0.84), and a = 0.3784 ± 0.0009 nm and c = 0.3292 ± 0.0002 nm for the (Ni,Pt)Al coating (c/a ≈ 0.87).

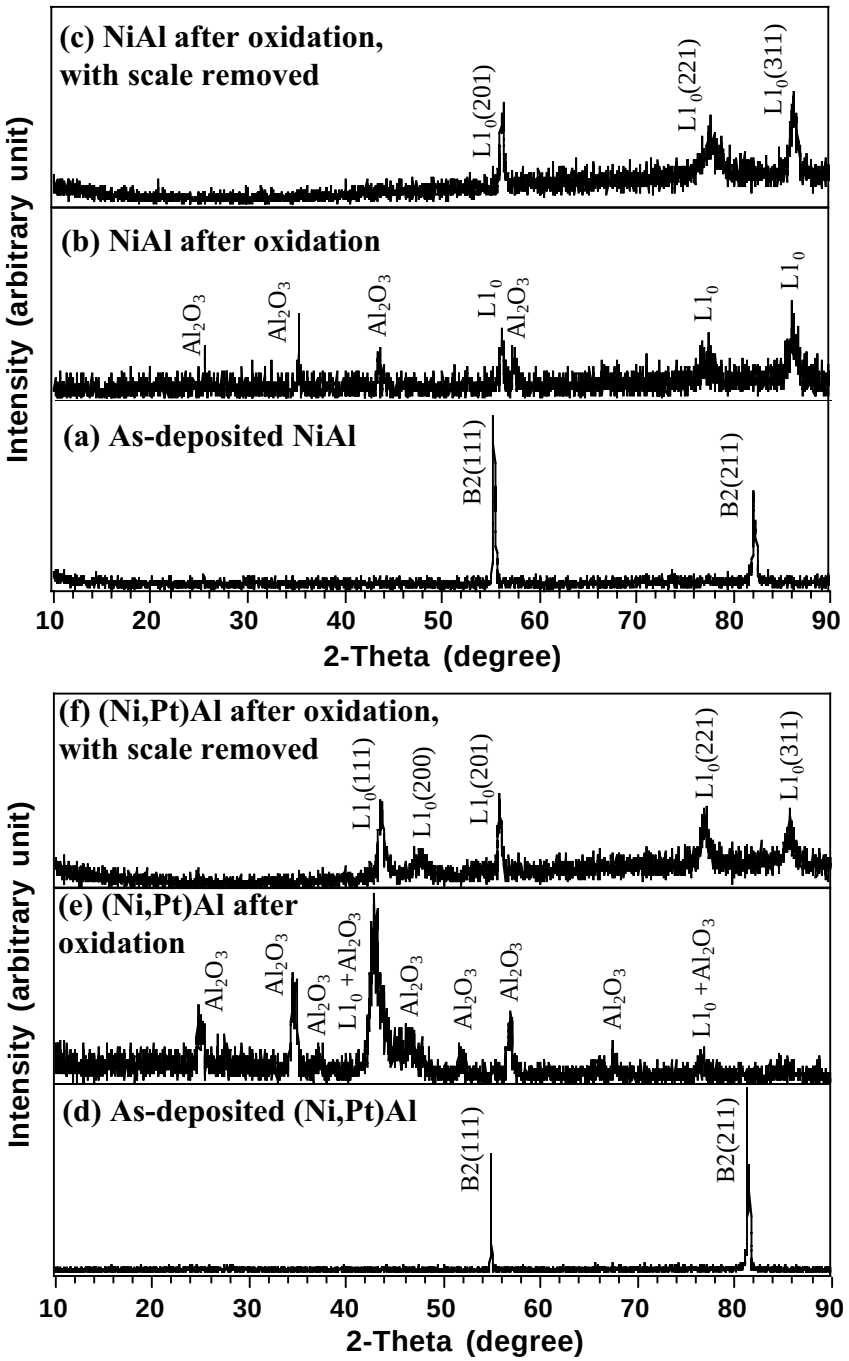

Fig. 22. XRD patterns of CVD NiAl and (Ni,Pt)Al coatings in the as-deposited conditions and after 100-h oxidation at 1150°C before and after oxide scales were removed: (a)-(c) NiAl, and (d)-(f) (Ni,Pt)Al.

** The lattice parameters were only measured for one NiAl coating specimen.

The etched microstructures of the bond coat specimens after cyclic oxidation (700 1-h cycles) at 1150°C are shown in Figure 23. Figure 23(a) is the SEM cross-section of the specimen with a YSZ top coat. After 700 cycles at 1150°C, Al depletion due to oxidation and interdiffusion produced a martensitic transformation of the β phase and the formation of γ′ precipitates in the coating layer, as marked by the arrows. The martensitic transformation also was observed in the remaining β phase on the other side of the same specimen without a top coat, Figure 23(b).

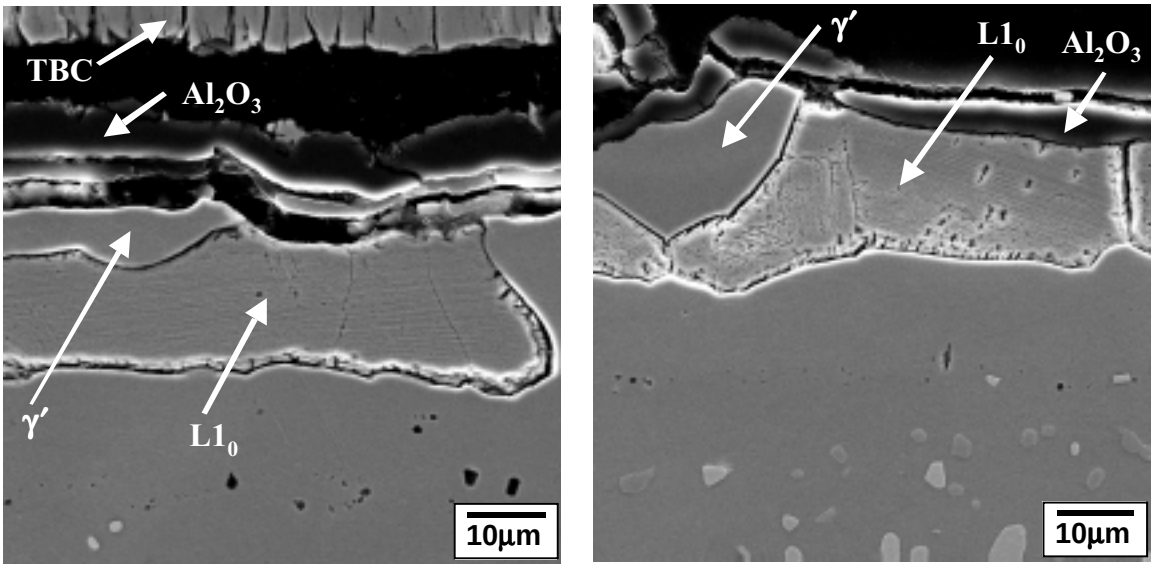

(a) (b)

Fig. 23. SEM cross-section of a coating specimen with (Ni,Pt)Al bond coat + TBC on one side and bond coat only on the other side after 700 cycles of oxidation at 1150°C: (a) the side with TBC, and (b) the side without TBC.

2.1.4. Discussion

The martensitic phase transformation in Ni-rich NiAl alloys has been extensively studied for more than 30 years.[69, 76-77] In the Ni-Al phase diagram, the B2 phase is stable over a wide composition region of 32-58at% Al at elevated temperatures and approximately 41-55at% Al at room temperature.[78] For the martensitic transformation to take place the following requirements must be satisfied:[69] (1) the Al content less than ~37at%;[79, 80] (2) the material exposed to elevated temperatures (> ~1000°C); (3) sufficiently fast cooling rates to suppress the $\beta \rightarrow \gamma'$ transformation. Quenching is not always necessary for the martensitic transformation to proceed, since it also occurs in alloys cooled in air,[70] which is quite similar to our present observation. The martensitic transformation temperature M_s has been found to be strongly dependent on the Ni concentration, varying from -200°C to 900°C.[76, 81-82]

Volume changes are commonly accompanied with martensitic transformations in Ni-Al alloys.[71, 74, 83] However, the reported values of the volume changes are somewhat

scattered, ranging from –2.32% to 1.94% for NiAl (36-40at% Al) alloys based on the calculations of the volumes of B2 and $L1_0$ unit cells; it is not clear if the lattice parameters used in the calculations were those near the M_s temperature. The volume change during the transformation of B2 to $L1_0$ was estimated in the present study using the room temperature lattice parameters, to be –2.05% for the NiAl and –2.25% for the (Ni,Pt)Al coating. It appears that the Pt incorporation slightly increased the volume change during the B2→$L1_0$ transformation. It should be noted that the lattice parameter of the B2 phase were determined from the as-coated specimens (~40at%Al), which could deviate from that after exposure (~32at% Al). Also, the lattice parameters of both B2 and $L1_0$ near the transformation temperature are needed to confirm this conclusion.

Surface rumpling was previously observed during cyclic oxidation of both simple aluminide and Pt-modified aluminide coatings on Ni-based superalloys.[73] Recent studies have shown renewed interest in surface roughening of (Ni,Pt)Al bond coatings, since it could possibly trigger TBC failure.[67, 84] A mechanism associated with the volume change during the β→γ' transformation has been proposed recently as the cause for rumpling of (Ni,Pt)Al coatings.[67] Although the calculated volume change (~38%) [67] may be questionable as the stoichiometry of β-NiAl was not taken into account, a phase-transformation-associated volume change could be likely responsible for the rumpling of the coating.

As indicated in Figure 4, cyclic oxidation accelerated Al depletion in the coating and thus promoted the β→γ' transformation, particularly along coating grain boundaries and/or underneath Al_2O_3 scales when more Al is consumed by scale spallation and re-formation during thermal cycling. However, the remaining β phase in the coating transformed to $L1_0$ during cooling. As the martensitic transformation of the β phase occurred prior to a significant amount of γ' precipitation near the coating surface area, the volume change associated with the martensitic transformation (both forward B2→$L1_0$ and reverse $L1_0$→B2) in a repeated mode could act as a precursor to initiate coating surface instability. This is in agreement with the surface roughness measurement by Lesnikova et al. [71] that the repeated martensitic transformation during thermal cycling led to an increase in the surface roughness of a simple NiAl coating. Further transformation of β to γ' might worsen the surface roughening. Alternatively, it has been suggested that a phase transformation caused macroscopic deformation of cast Ni-35.5at%Al [85] and Ni-34.7at%Al-5.7Pt+Hf during cyclic oxidation testing at 1100°C-1200°C.[86] Moreover, a recent high-temperature XRD study on cast Ni-Al and (Ni,Pt)-Al has indicated that alloys with a $L1_0$ + γ' structure at room temperature undergo a reversible transformation to single phase β when heated to 1100°C.[86] Thus the γ' observed after cooling may not be present at the cycle temperature.

It has been recognized that certain alloying elements, such as Ti, Cr, Mo, Ta, W, and Si, act as β stabilizers with regard to the β→$L1_0$ transformation, thereby lowering the M_s temperature.[81, 87] Other elements, such as Co, destabilize the β phase and raise the M_s temperature. As shown in Table 6, the alloying elements, e.g., Co, Cr and some refractory metals, diffused into the NiAl or (Ni,Pt)Al coating layer during aluminizing

process and the subsequent oxidation exposure, which might stabilize the β phase in the inter-diffusion zone, Figure 1. The incorporation of alloying elements further complicates the issue of martensitic transformations in TBC bond coats by affecting the M_s temperature.

2.1.5. Conclusions

Transformation from a β phase (B2) to a martensitic phase ($L1_0$) was observed in single-phase NiAl and (Ni,Pt)Al bond coats when the coating specimens were cooled from 1150°C after isothermal and/or cyclic oxidation tests. The martensitic transformation occurred when Al was depleted by the formation of the Al_2O_3 scale and the interdiffusion between the coating and superalloy substrate during high-temperature exposure. Furthermore, the transformation of the coating to martensite occurred prior to the transformation to γ' near the coating surface. Volume changes commonly associated with the martensitic transformation likely contribute to the early stage of surface roughening, which is of interest because deformation of the bond coat can initiate failure of TBCs.

2.2. Cyclic Oxidation Behavior of Bare and Aluminized Ni-based Superalloys with Various Hf Contents

2.2.1. Introduction

State-of-the-art TBC systems, which are used to protect superalloy components in the hot section of gas turbine engines, typically consist of an oxidation-resistant metallic bond coat overlaid with a thermally insulating ceramic top layer. Aluminide coatings, NiAl or (Ni,Pt)Al are commonly used as bond coatings for TBC systems that utilize EB-PVD ceramic top coats.[88] The oxidation resistance of the metallic bond coat is based on its ability to form a protective, external Al_2O_3 scale. The thermomechanical stability of the alumina scale is the factor that most often limits the durability of current EB-PVD TBC systems.[88-90] In the present study, the cyclic oxidation behavior of a directionally-solidified (DS) Ni-based superalloy René 142 with various Hf contents was studied with a focus on the effect of reactive element Hf on oxidation resistance. The DS alloy René 142 is chosen as the substrate alloy primarily because it is widely used in many applications and less expensive as compared with single-crystal superalloys, particularly when considered for large-sized components in land-base turbine engines.[91]

2.2.2. Experimental Procedures

Three versions of DS René 142 superalloy were cast by PCC and the alloy compositions are given in Table 7. The Hf content was the primary difference in the three alloys. Hafnium in alloys A, B and C was 0.02 wt.%, 0.76 wt.% and 1.37 wt.%, respectively. The sulfur content of the alloys is not known at this time, but it is expected to be relatively high based on the oxidation performance of the alloys.

Specimens of the three alloys were CVD aluminized (6h at 1100°C in a laboratory scale reactor at ORNL to form a single-phase NiAl coating. All specimens were polished to a 0.3mm alumina finish and were ultrasonically cleaned in acetone and methanol prior to CVD coating or oxidation tests. Cyclic oxidation testing was conducted in an automated furnace rig at 1150°C in dry, flowing O_2. Each cycle consisted of a 1-h exposure at 1100 and 1150°C in air followed by a 10-min cooling. Before and after exposure, selected specimens were examined by light microscopy, FEG-SEM equipped with EDS. The corrosion products on specimens for cross-sectional examination were protected by Cu-plating the specimen prior to mounting in epoxy.

2.2.3. Results and Discussion

2.2.3.1. 1150°C Oxidation Test of René 142 Superalloys

Preliminary oxidation testing of this alloy was conducted at 1150°C in order to provide a baseline comparison of oxidation performance with single-crystal René N5. Four specimens were tested at 1150°C: one of each composition and a fourth specimen of the B composition (0.76 Hf) that had been pre-oxidized in a low p_{O2} environment (Ar + H_2) to form a thin layer of pure alumina.

Table 7. The compositions (in wt.%) of three René 142 superalloys measured by X-ray fluorescence spectroscopy (XRF).

Element	Mold 1(A)	Mold 2(B)	Mold 3 (C)
Si	<0.02	<0.02	<0.02
Mn	<0.01	<0.01	<0.01
P	<0.005	<0.005	<0.005
Cr	6.82	6.73	6.65
Mo	1.49	1.48	1.47
Fe	0.03	0.03	0.03
Ti	<0.02	<0.02	<0.02
Al	**6.12**	**6.13**	**6.06**
Co	11.85	11.78	11.71
W	4.8	4.79	4.84
V	<0.01	<0.01	<0.01
Cu	<0.01	<0.01	<0.01
Zr	<0.007	0.007	0.021
Nb	<0.02	<0.02	<0.02
Ta	6.43	6.34	6.28
Re	2.83	2.82	2.8
Hf	**0.02**	**0.76**	**1.37**
Y	<0.02	<0.02	<0.02
Pt	NA	<0.1	<0.1
Pd	NA	<0.1	<0.1

Each of the four René 142 alloys experienced significant oxide spallation after only 20 1-h cycles at 1150°C in oxygen. The specimen surfaces were blue-green in appearance with much loosely adhered oxide. By comparison, René N5 remained a uniform grey appearance with no flaking of oxide until hundreds of cycles at 1150°C. Thus, it is obvious that the oxidation resistance of these three René 142 alloys is significantly inferior to that of the single-crystal René N5 alloys. Testing of these alloys was discontinued after 20 1-h cycles due to their poor oxidation behavior.

2.2.3.2. 1100°C Oxidation Test of René 142 Superalloys

A second set of oxidation tests on the three versions of René 142 was conducted at 1100°C. Figure 24 shows the mass changes during 100 1-h cycles at 1100°C in oxygen. All three alloys continuously lost mass during the cyclic oxidation test. The alloys B and C had noticeably better performance than the alloy A. The alloy C, with the highest Hf level (1.37 wt.%), showed the best performance. Again, testing of these alloys at 1100°C was discontinued after 100 1-h cycles due to poor oxidation resistance.

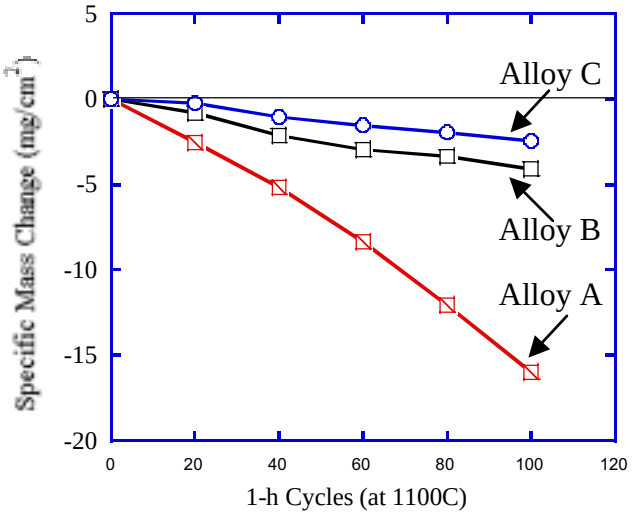

Fig. 24. The mass changes of René 142 specimens with different Hf contents during 1-h cycles at 1100°C.

2.2.3.3. 1150°C Oxidation Test of CVD Aluminized René 142 Superalloys

The as-coated CVD NiAl coating on René 142 consisted of large aluminide grains (~ 50-100 μm) outlined with a distinct network of prominent grain boundary ridges on the coating surface, Figure 25(a), which was very similar to the CVD NiAl coatings formed on single-crystal René N5.[9] The coating thickness measured from the original substrate surface was ~25 μm, as shown in Figure 25(b). There was an interdiffusion zone (~ 25 μm) formed between the coating and substrate where the light finger-like phases were the topologically-close packed (TCP) phases, Figure 25(b). The EPMA composition profiles indicated that the Al was ~40 at.% through the coating thickness, and there was significant incorporation of alloying elements, such as Co and Cr, from the substrate into the NiAl coating, Figure 25(c). These specimens were then tested at 1150°C in 1-h cycles in oxygen. After 20 cycles the coatings on the alloys A and B were blue in appearance, with evidence of spallation occurring from the alloy A. The alloy C (highest Hf) was grey in appearance, with evidence of slight amounts of spallation. Thus, the behavior of these coatings was proportional to the Hf content of the substrate, with higher Hf levels resulting in improved performance. By comparison, some CVD aluminized René N5 alloys remained intact after up to 500 cycles at 1150°C. The surface morphology of the coated René 142 after 100 1-h cycles is shown in Figure 26, indicating severe spallation of oxide scales.

2.2.4. Summary

The DS René 142 superalloys with three Hf contents were evaluated with cyclic oxidation tests at 1100 and 1150°C with and without NiAl coatings. Poor scale adhesion was observed on bare René 142 superalloys and NiAl-coated alloys. Spallation occurred at relatively early stages disregarding the Hf contents in the alloys, which was not as expected. More characterization is needed to explain the poor oxidation behavior of

these specimens with particular focus on the impurity levels such as sulfur content in the coating specimens.

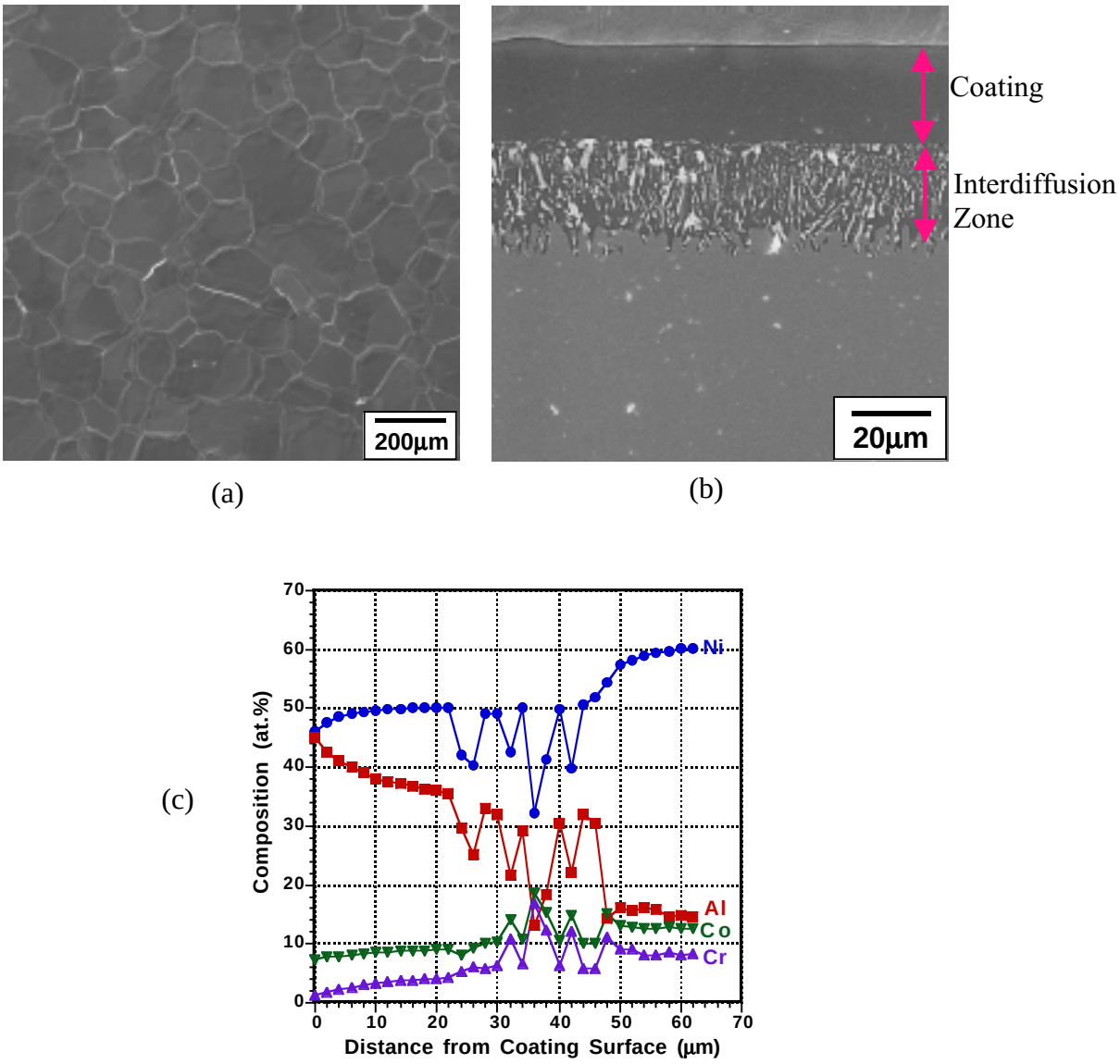

Fig. 25. SEM secondary electron images of (a) surface morphology and (b) cross-section of the as-deposited CVD NiAl coating on René 142, and (c) compositional profiles of major elements measured by EPMA through the thickness of the NiAl coating.

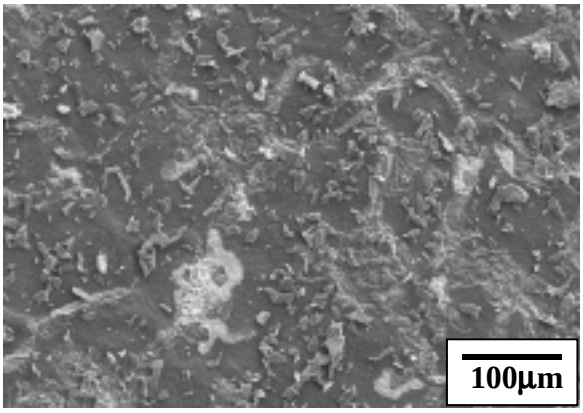

Fig. 26. SEM secondary electron image of surface morphology of NiAl-coated René 142 superalloy after 100 1-h cycles at 1150°C.

2.3. Electroplating of Pt in a Laboratory Plating System

2.3.1. Introduction

NiAl or (Ni,Pt)Al coatings are commonly used as bond coats for EB-PVD TBC systems.[88] The adhesion of the protective Al_2O_3 scale formed on top of the bond coat is one of the predominant factors that affect TBC lifetime.[88-90] It has been a common industrial practice to incorporate Pt in the aluminide coating to improve Al_2O_3 scale adherence.[92, 93] A platinum plating system has been set up at Tennessee Technological University (TTU) to provide an avenue to carefully control the Pt plating process for synthesizing (Ni,Pt)Al and other Pt-containing coating systems. The effects of the Pt electroplating parameters such as plating current density on Pt adhesion and uniformity have been investigated.

2.3.2. Experimental Procedures

Figure 27 shows the laboratory plating system, which includes a polyvinylidene fluoride (PVDF) plating tank (35.6cm x 25.4cm x 25.4cm), a Teflon immersion heater, an in-tank filter system, and a DC power source supplied by a rectifier with up to 3 amps and 18 volts DC output. A close-up view of the plating tank in Figure 27(b) shows the anode and cathode bars. The plastic balls floating on top of the solution are to prevent evaporation of the solution during plating. The Ni-based superalloy specimens, such as René 80 (18 x 14 x 1.5 mm) and René 142 coupons (ϕ15mm x 1.5 mm) were used as the substrate alloys. The plating was performed using the Pt20-Q electrolyte [94] ("Q" salt, Johnson Matthey) at 90-95°C with a solution pH of 10-10.5 and Pt concentration greater than 10 g/l. A number of parameters, such as surface condition, edge/corner roundness, current density, were varied and their effects on Pt-layer quality were determined.

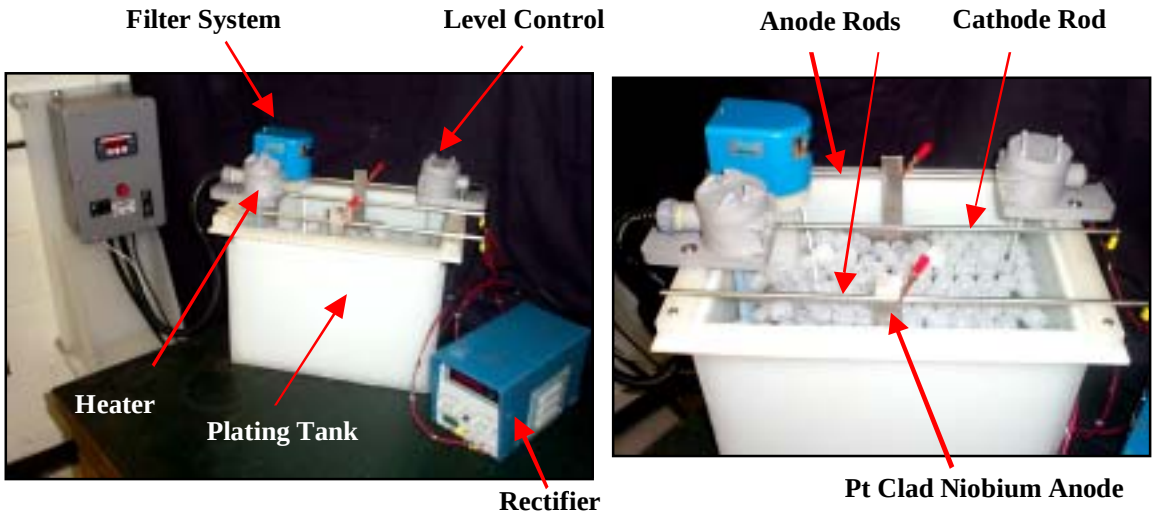

Fig. 27. The laboratory platinum plating system at TTU.

The specimens were grit blasted using Al_2O_3 and ultrasonically cleaned in hot water, acetone and methanol prior to Pt plating. The mass changes before and after plating were recorded.

2.3.3. Results and Discussion

2.3.3.1. Effect of Electroplating Current Density on Pt Plating Rate

During the first several plating runs, spallation on specimen edges was noticed when the plating current density was set up at 0.6A/dm^2. In order to improve the adhesion of the Pt layer, several steps were taken, including the following: (1) to round the edges and corners by grinding prior to grit blasting, (2) to ensure a thorough grit blasting particularly near the edges and a thorough cleaning, and (3) to lower the plating current density while maintaining the reasonable plating rate.

Spallation occurred again when the edges and corners of the specimen were rounded and careful grit blasting and cleaning were applied if the current density was kept at the ~0.6A/dm^2. When the current density was reduced from 0.6 to 0.3A/dm^2, spallation was eliminated and the Pt layer was adherent all around the specimen surface. The corresponding plating time for a 6μm thick Pt layer was increased from 45min to 100min with the reduction in current density. This process was reproducible with very consistent plating rate. The typical surface morphology and the cross-section of the as-plated Pt were examined by SEM, as shown in Figure 28.

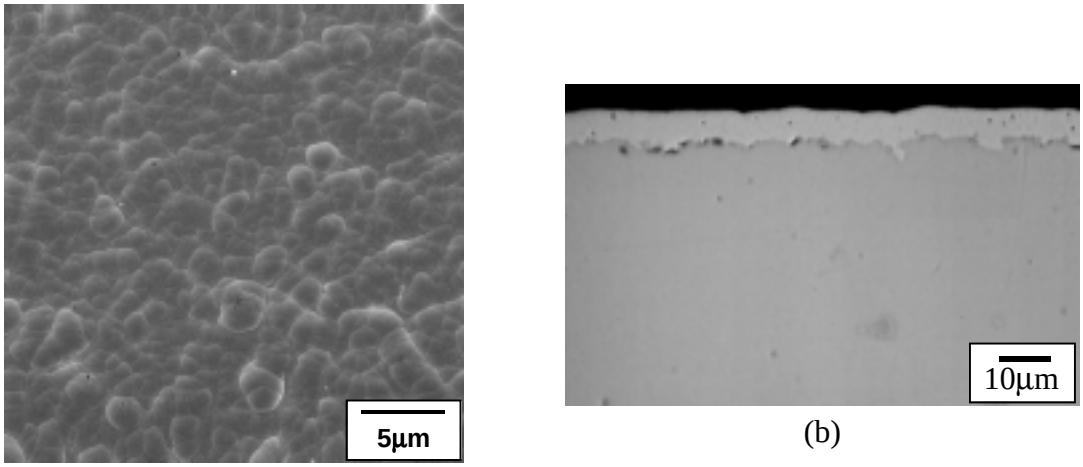

(a) (b)

Fig. 28. (a) SEM secondary image of the Pt surface, (b) optical micrograph of the cross-section of the as-plated Pt layer. (current density = 0.3A/dm^2; plating time = 100-120min)

A variety of plating current densities were used to investigate its effect on Pt plating rate and Pt uniformity. René 80 superalloy coupons of identical size (18 x 14 x 1.5 mm) were used as the substrates to prevent any disparity that might arise from specimen size or geometry. The correlation between plating current density and plating rate is shown in Figure 29. When the current density was reduced from 0.6A/dm^2 to

0.3A/dm^2, the plating rate decreased from ~0.14 μm/min to ~0.07 μm/min, as expected. When the current density was further reduced to 0.2A/dm^2, a plating rate of 0.04μm/min was recorded. As shown in Figure 29, a linear relationship was found between the plating current density and plating rate. Such information is particularly useful in predicting the required plating time to achieve certain thickness if the plating current is known.

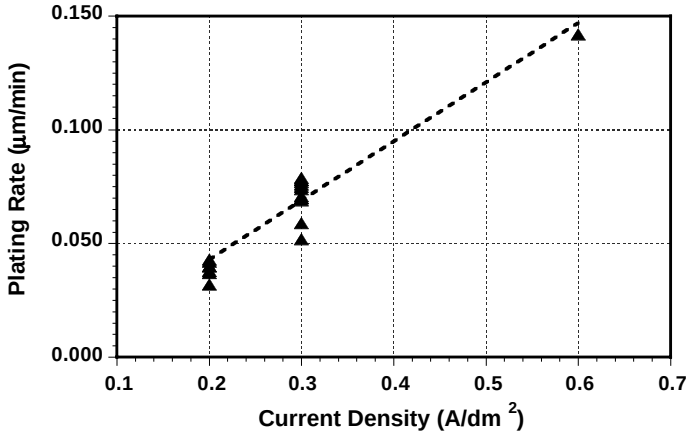

Fig. 29. The effect of plating current density on plating rate.

2.3.3.2. Effect of Electroplating Current Density on Pt Thickness Distribution

The distribution of Pt thickness through the specimen was examined. Eight readings at different locations were taken for each specimen, as indicated in Figure 30(a); locations #1-#6 were on the specimen surface, and #7 and #8 were near the edges. The average of the six readings (#1-#6) was taken as the thickness of the Pt on the flat surface, and the average of two readings (#7 and #8) was used as the thickness near the edges. When the plating was performed with a current density of 0.6A/dm^2, the ratio of the Pt thickness near specimen edges to that on the surface was ~2.7, i.e., more Pt was built up near the edges than on the flat surface. This also explained why the Pt layer had a tendency to crack or spall, particularly on specimen edges when a high current density was used. The thicker Pt on the specimen edges led to higher internal stress and thus cracking and spallation. Edge-to-surface thickness ratios of approximately 1.7 and 1.3 were observed when the current densities were decreased to 0.3A/dm^2 and 0.2A/dm^2, respectively.

Based on such results a plating current density of 0.2A/dm^2 was identified as the appropriate current density for obtaining an adherent Pt layer with a relatively uniform thickness distribution and at a reasonable plating rate. Several René 142 superalloy coupons were plated by using the identified plating parameters. The electroplated Pt was uniform and with metallic shininess. No spallation was observed after Scotch tape test, indicating reasonably good adherence. Selected Pt-plated René 142 specimens also were aluminized in a low-activity CVD reactor. Some blisters were noticed on the surface of the CVD platinum aluminide coatings. SEM surface morphology suggests that these blisters exist near the coating surface area without penetration into the coating interior. A

post-plating annealing treatment prior to the CVD aluminizing process is being considered to reduce residual stress and therefore further improve adherence of the electro-plated Pt layer.

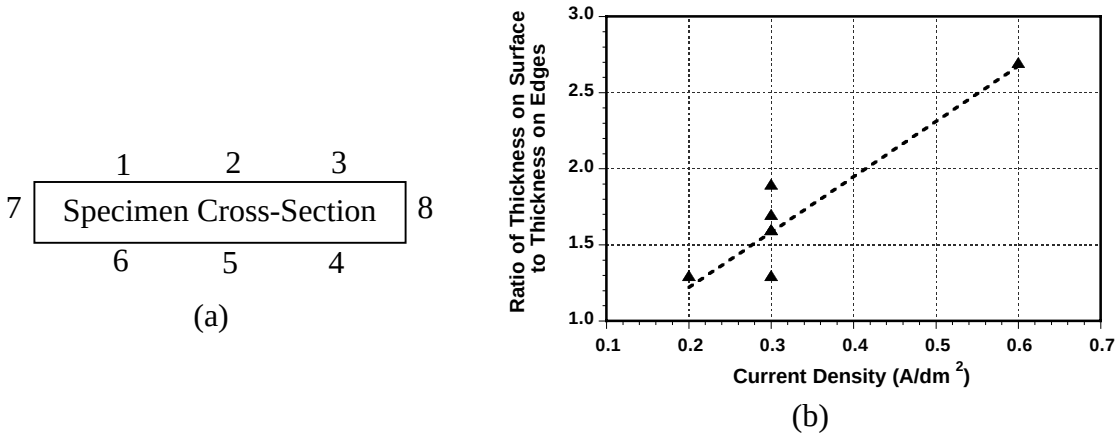

Fig. 30. The effect of plating current density on Pt thickness distribution, (a) schematic showing the eight locations where thickness readings were taken, and (b) the correlation between the plating current density and the thickness distribution (the ratio of the thickness on the specimen surface to the thickness on the edges).

2.3.4. Summary

The effects of electroplating parameters on Pt coating quality were investigated with the focus on plating current density which was believed to affect not only the plating rate but also Pt adhesion. The current densities ranging from 0.2 to 0.6A/dm^2 were used in a laboratory plating system at TTU. While the plating rate increased nearly linearly with the current density, more Pt tended to build up near the specimen edges/corners than on the flat surface. The thicker Pt on specimen edges/corners led to greater internal stress and therefore spallation in these areas.

3. Acknowledgements

The author would like to acknowledge K. M. Cooley, G. Garner, L. D. Chitwood, L. R. Walker, and K. S. Thomas at ORNL, W. E. Hawkins, D. A. Walker, R. L Grills, L. W. Yeary and A. Liu at TTU for assisting with the experimental work; C. Kortovich and L. Graham at PCC Airfoils, B. Warnes and N. DuShane at Howmet Corporation for supplying some of the alloys. Thanks are also extended to J. A. Nesbitt at NASA Glenn Research Center for providing the COSIM computer model. This research was sponsored by the U.S. Department of Energy, Fossil Energy Advanced Materials Research Program, under contract DE-AC05-00OR22725 with UT-Battelle LLC and subcontract 4000007035 with Tennessee Technological University.

4. References

1. G. C. Wood, I. G. Wright, T. Hodgkiess, and D. P. Whittle, *Werk. Korr.* 21 (1970) 900.
2. B. A. Pint and J. M. Rakowski, *NACE Paper 00-259*, Houston, TX, presented at NACE Corrosion 2000, Orlando, FL, March 2000.
3. P. F. Tortorelli and J. H. DeVan, *Mat. Sci. Eng.*, A153 (1992) 573.
4. J. H. DeVan and P. F. Tortorelli, *Corr. Sci.*, 35 (1993) 1065.
5. P. F. Tortorelli and K. Natesan, *Mater. Sci. Eng.*, A258 (1998) 115.
6. B. A. Pint, P. F. Tortorelli, and I. G. Wright, *Mater. High Temp.*, 16 (1999) 1.
7. B. A. Pint, Y. Zhang, P. F. Tortorelli, J. A. Haynes, and I. G. Wright, *Mater. High Temp.*, 18 (2001) 185.
8. F. D. Geib and R. A. Rapp, in *Processing and Fabrication of Advanced Materials for High Temperature Applications*, Eds. V. A. Ravi and T. S. Srivatsan, TMS, 1992, pp. 347.
9. W. Y. Lee, Y. Zhang, I. G. Wright, B. A. Pint, and P. K. Liaw, *Metall. Mater. Trans.*, 29A (1998) 833.
10. R. Bianco and R. A. Rapp, in *Metallurgical and Ceramic Protective Coatings,* Ed. K. H. Stern, Chapman & Hall, 1996, pp. 237.
11. N. V. Bangaru and R. C. Krutenat, *J. Vac. Sci. Technol.*, 2B (1984) 806.
12. Y. Zhang, B. A. Pint, J. A. Haynes, K. M. Cooley, and I. G. Wright, in *Proc. Seventeenth Annual Conf. Fossil Energy Materials*, R. R. Judkins (comp.), U.S. Department of Energy, 2003.
13. B. A. Pint, Y. Zhang, P. F. Tortorelli, J. A. Haynes, and I. G. Wright, in *Proc. Sixteenth Annual Conf. Fossil Energy Materials*, R. R. Judkins (comp.), U.S. Department of Energy, 2002.
14. F. H. Stott, G. C. Wood, and J. Stringer, *Oxid. Met.*, 44 (1995) 113.
15. G. C. Wood and D. P. Whittle, *Corr. Sci.*, 7 (1967) 763.
16. J. C. Colson and J. P. Larpin, *MRS Bulletin*, Oct. (1994) 23.
17. G. V. Samsonov, *Oxide Handbook*, IFI/Plenum, New York, 1973.
18. Zs. Tokei, K. Hennesen, H. Viefhaus, and H. J. Grabke, *Mater. Sci. Tech.*, 16 (2000) 1129.
19. P. Kofstad, in *High Temperature Corrosion*, Elsevier Applied Science, London, 1987, pp. 105.
20. H. Nickel, Y. Wouters, M. Thiele, and W. J. Quadakkers, *Fresenius J. Anal. Chem.*, 361 (1998) 540.
21. H. Asteman, J.-E. Svensson, L.-G. Johansson, and M. Norell, *Oxid. Met.*, 52 (1999) 95.
22. H. Asteman, J.-E. Svensson, M. Norell, and L.-G. Johansson, *Oxid. Met.*, 54 (2000) 11.
23. K. N. Strafford and R. Manifold, *Corr. Sci.*, 9 (1969) 489.
24. J. C. Colson and J. P. Larpin, *Mater. Sci. Eng.*, 87 (1987) 11.

25. A. Hashimoto, *Geochimi. Cosmochimi. Acta*, 56 (1992) 511.

26. E. J. Opila and N. S. Jacobson. in *Electrochemical Society Proceedings*, 96-26, 1996, pp. 269.

27. D. L. Douglass, P. Kofstad, A. Rahmel, and G. C. Wood, *Oxid. Met.*, 45 (1996) 529.

28. I. Kvernes, M. Oliveira, and P. Kofstad, *Corr. Sci.*, 17 (1977) 237.

29. H. Buscail, S. Heinze, P. Dufour, and J. P. Larpin, *Oxid. Met.*, 47 (1997) 445.

30. J. L. Smialek, *Metall. Trans.*, 22A (1991) 739.

31. D. R. Sigler, *Oxid. Met.*, 40 (1993) 555.

32. M. A. Smith, W. E. Frazier, and B. A. Pregger, *Mater. Sci. Eng.*, 203A (1995) 388.

33. R. Janakiraman, G. H. Meier, and F. S. Pettit, *Metall. Mater. Trans.*, 30A (1999) 2905.

34. J. L. Smialek, *Metall. Trans.*, 9A (1978) 309

35. B. A. Pint, P. F. Tortorelli, I. G. Wright, J. A. Haynes, and W. Y. Lee, in *Proc. Fourteenth Annual Conf. Fossil Energy Materials*, R. R. Judkins (comp.), U.S. Department of Energy, 2000.

36. B. A. Pint and R. Peraldi, *ASME Paper #GT2003-38692*, presented at the International Gas Turbine & Aeroengine Congress & Exhibition, Atlanta, GA, June 2-5, 2003.

37. J. A. Nesbitt, *NASA/TM — 2000-209271* (2000).

38. R. W. Heckel, M. Yamada, C. Ouchi, and A. J. Hickl, *Thin Solid Films*, 45 (1977) 367.

39. S. R. Levine, *Metall. Trans.*, 9A (1978) 1237.

40. J. E. Morral, *Surf. Coat. Technol.*, 43/44 (1990) 371.

41. S. Datta, R. Filipek, and M. Danielewski, *Defect Diffus. Forum*, 203-205 (2002) 47.

42. H. C. Akuezue and D. P. Whittle, *Met. Sci.*, 17 (1983) 27.

43. P. C. Tortorici and M. A. Dayananda, *Mater. Sci. Eng.*, 244A (1998) 207.

44. Y. Zhang and B.A. Pint, in *Proc. Sixteenth Annual Conf. Fossil Energy Materials*, R. R. Judkins (comp.), U.S. Department of Energy, *April 22-24, Baltimore, Maryland, 2002*.

45. J. A. Nesbitt and R. W. Heckel, *Metall. Trans.*, 18A (1987) 2075.

46. C. E. Lowell, C. A. Barrett, R. W. Palmer, J. V. Auping, and H. B. Probst, *Oxid. Met.*, 36 (1991) 81.

47. J. L. Smialek and J. V. Auping, *Oxid. Met.*, 57 (2002) 559.

48. L. Onsager, *Phys. Rev.*, 37 (1931) 405.

49. J. S. Kirkaldy, *Can. J. Phys.*, 36 (1958) 899.

50. M. S. Thompson, J. E. Morral, and A. D. Romig, Jr, *Metall. Trans.*, 21A (1990) 2679.

51. Y. H. Son and J. E. Morral, *Scripta Metall. Mater.*, 28 (1993) 833.

52. M. A. Dayananda, *Metall. Trans.*, 27A (1996) 2504.

53. Landolt-Börnstein, in *Numerical Data and Functional Relationships in Science and Technology*, New Series, Group III, Vol. 26, Diffusion in Solid Metals and Alloys, Ed. H. Mehrer, Springer-Verlag Berlin Heidelberg, 1990, pp. 343.

54. M. Weinhagen, B. Köhler, J. Wolff, and Th. Hehenkamp, *Defect Diffus. Forum*, 143-147 (1997) 449.

55. H. C. Akuezue and J. Stringer, *Metall. Trans.*, 20A (1989) 2767.

56. R. Sivakumar and E. J. Rao, *Oxid. Met.*, 17 (1982) 391.

57. W. T. Tsai and K. E. Huang, *Thin Solid Films*, 366 (2000) 164.

58. Y. H. Sohn and M. A. Dayananda, *Metall. Mater. Trans.*, 33A (2002) 3375.

59. T. Helander and J. Agren, *Acta mater.*, 47 (1999) 3291.

60. S. K. Mannan, V. Seetharaman, and V. S. Raghunathan, *Mater. Sci. Eng.*, 60A (1983) 79.

61. A. R. Marder, J. R. Regina, and J. N. Dupont, in *Proc. Sixteenth Annual Conf. Fossil Energy Materials*, R. R. Judkins (comp.), U.S. Department of Energy, 2002.

62. B. A. Pint, Y. Zhang, J. A. Haynes, and I. G. Wright, in *Proc. Seventeenth Annual Conf. Fossil Energy Materials*, R. R. Judkins (comp.), U.S. Department of Energy, April 22-24, Baltimore, Maryland, 2003.

63. B. M. Warnes and D. C. Punola, *Surf. Coat. Technol.*, 94-95 (1997) 1.

64. B. A. Pint, I. G. Wright, W. Y. Lee, Y. Zhang, K. Prüβner, and K. B. Alexander, *Mater. Sci. Eng.*, 245A (1998) 201.

65. Y. Zhang, W. Y. Lee, J. A. Haynes, I. G. Wright, B. A. Pint, K. M. Cooley, and P. K. Liaw, *Metall. Mater. Trans.*, 30A (1999) 2679.

66. M. Gell, K. Vaidyanathan, B. Barber, J. Cheng, and E. Jordan, *Metall. Mater. Trans.*, 30A (1999) 427.

67. V. K. Tolpygo and D. R. Clarke, *Acta mater.*, 48 (2000) 3283.

68. Z. Mutasim and W. Brentnall, *ASME Paper No. 96-GT-436*, ASME, New York, NY, 1996

69. S. Rosen and J. A. Goebel, *Trans. TMS-AIME*, 242 (1968) 722.

70. J. L. Smialek, *Metall. Trans.*, 2 (1971) 913.

71. E. G. Lesnikova and V. P. Lesnikov, *Met. Sci. Heat Treat.*, 28 (1986) 372.

72. A. Dent, S. B. Newcomb, and W. M. Stobbs, in *Inst. Phys. Conf.* Ser. No. 138: Section 9, Electron Microscopy and Analysis, 138 (1993) 429.

73. P. Deb, D. H. Boone, and T. F. Manley, *J. Vac. Sci. Technol.*, A 5(6) (1987) 3366.

74. V. S. Litvinov, L. P. Zelenin, and R. Sh. Shklyar, *Fiz. Metal. Metalloved.*, 31 (1971) 137.

75. Y. Zhang, J. A. Haynes, W. Y. Lee, I. G. Wright, B. A. Pint, K.M. Cooley, and P.K. Liaw, *Metall. Mater. Trans.*, 32A (2001) 1727.

76. Y. K. Au and C. M.Wayman, *Scripta Metall.*, 6 (1972) 1209.

77. P. L. Potapov, S. Y. Song, V. A. Udovenko, and S. D. Prokoshkin, *Metall. Trans.*, 28A (1997) 1133.

78. Binary Alloy Phase Diagrams, Second Edition, Eds., T.B. Massalski, H. Okamoto, P.R. Subramanian, L. Kacprzak, ASM, 1990, pp. 181.

79. K. S. Kumar, S. K. Mannan, R. K. Viswanadham, *Acta mater.*, 40 (1992) 1201.

80. A. S. Murthy and E. Goo, *Acta mater.*, 41 (1993) 3435.

81. J. L. Smialek and R. F. Hehemann, *Metall. Trans.*, 4 (1973) 1571.

82. R. Kainuma, H. Ohtani, and K. Ishida, *Metall. Trans.*, 27A (1996) 2445.

83. P. S. Khadkikar, I. E. Locci, K. Vedula, and G. M. Michal, *Metall. Trans.*, 24A (1993) 83.

84. R. C. Pennefather and D. H. Boone, *Surf. Coat. Technol.*, 76-77 (1995) 47.

85. J. Doychak, J. L. Smialek, and C. A. Barrett, in *Oxidation of High Temperature Intermetallics*, Eds. T. Grobstein and J. Doychak, Warrendale, PA, The Minerals, Metals and Materials Society, 1989, pp. 41.

86. B. A. Pint, C. J. Rawn, E. A. Payzant and I. G. Wright, Oak Ridge National Laboratory, manuscript in progress, 2002.

87. V. S. Litvinov and Ye. G. Lesnikova, *Fiz. Metal. Metalloved.*, 44 (1977) 1297.

88. P. K. Wright, *Mater. Sci. Eng.*, 245A (1998) 191.

89. S. M. Meier, D. M. Nissley, K. D. Sheffler, S. Bose, *J. Eng. Gas Turbine Power*, 112 (1990) 522.

90. J. A. Haynes, Y. Zhang, W. Y. Lee, B. A. Pint, I. G. Wright, and K. M. Cooley, in *Elevated Temperature Coatings: Science and Technology III*, Eds. J. M. Hampikian and N. B. Dahotre, The Minerals, Metals & Materials Society, 1999, pp. 185.

91. E. W. Ross and K. S. O'Hara, in *Superalloys 1992*, Eds. S. D. Antolovich, R. W. Stusrud, R. A. MacKay, D. L. Anton, T. Khan, R. D. Kissinger, D. L. Klarstrom, TMS, 1992, pp. 257.

92. G. Lehnert and H. Meinhard, *Elctrocdep. Surf. Treat.*, 1 (1972-1973) 189.

93. J. S. Smith and D. H. Boone, *ASME Paper No. 90-GT-319*, ASME, New York, NY, 1990.

94. J. M. Albon, W. J. Davis, P. E. Skinner, and S. G. Warren, *US Patent* 5,102,509, 1992.